Measurement of analyzing powers of π^+ and π^- produced on a hydrogen and a carbon target with a 22-GeV/c incident polarized proton beam

C. E. Allgower,* K. W. Krueger, T. E. Kasprzyk, H. M. Spinka, D. G. Underwood, and A. Yokosawa
Argonne National Laboratory, Argonne, Illinois 60439

G. Bunce, H. Huang, Y. Makdisi, T. Roser, and M. Syphers†
Brookhaven National Laboratory, Upton, New York 11973

A. A. Derevschikov, Yu. A. Matulenko, L. V. Nogach, S. B. Nurushev, and A. N. Vasiliev
Institute for High Energy Physics, Protvino 142284, Russia

M. Bai and S. Y. Lee
Indiana University, Bloomington, Indiana 47405

Y. Goto, N. Hayashi, T. Ichihara, M. Okamura, and N. Saito
RIKEN, The Institute of Physical and Chemical Research, Wako, Saitama 351-0198, Japan

H. En'yo, K. Imai, Y. Kondo, Y. Nakada,‡ M. Nakamura, and H. Saito
Kyoto University, Kyoto, Japan

H. Sakai, T. Wakasa,§ and K. Yako
University of Tokyo, Hongo 7-3-1, Bunkyo, Tokyo 113-0033, Japan

V. Baturine‖ and A. Ogawa
Pennsylvania State University, University Park, Pennsylvania 16802

V. Ghazikhanian, G. Igo, S. Trentalange, and C. Whitten
University of California at Los Angeles, Los Angeles, California 90095

N. I. Belikov and A. I. Pavlinov
Wayne State University, Detroit, Michigan 48202

(E925 Collaboration)
(Received 11 September 2001; published 20 May 2002)

The analyzing powers of π^+ and π^- were measured using an incident 22-GeV/c transversely polarized proton beam at the Brookhaven Alternating Gradient Synchrotron. A magnetic spectrometer measured $\pi^\pm$ inclusive asymmetries on a hydrogen and a carbon target. An elastic polarimeter with a CH_2 target measured *pp* elastic-scattering asymmetries to determine the beam polarization using published data for the *pp* elastic analyzing power. Using the beam polarization determined from the elastic polarimeter and asymmetries from the inclusive spectrometer, analyzing powers A_N for $\pi^\pm$ were determined in the x_F and p_T ranges (0.45–0.8) and (0.3–1.2 GeV/c), respectively. The analyzing power results are similar in both sign and character to other measurements at 200 and 11.7 GeV/c, confirming the expectation that high-energy pion inclusive analyzing powers remain large and relatively energy independent. This suggests that pion inclusive polarimetry may be a suitable method for measuring future beam polarizations at BNL RHIC or DESY HERA. Analyzing powers of π^+ and π^- produced on hydrogen and carbon targets are the same. Various models to explain inclusive analyzing powers are also discussed.

DOI: 10.1103/PhysRevD.65.092008 PACS number(s): 13.88.+e, 13.85.Ni

I. INTRODUCTION

In the past, high-energy single transverse spin asymmetries were expected to be small [1]. However, the Fermilab E704 experiment found large spin effects in the reactions $p_\uparrow p \to \pi^+ X$ and $p_\uparrow p \to \pi^- X$ at 200 GeV/c or $\sqrt{s} = 19.4$ GeV in the beam fragmentation region [2]. As shown in Fig. 1, a striking dependence in Feynman x (x_F) was observed in which the analyzing power A_N increased from 0 to about 0.3 with increasing x_F for the π^+ data and decreased from 0 to about -0.3 with increasing x_F for the π^-

*Present address: Indiana University Cyclotron Facility, Indiana University, Bloomington, IN 47405.

†Present address: Fermi National Accelerator Laboratory, Batavia, IL 60510.

‡Present address: Toshiba Corporation, Tokyo, Japan.

§Present address: Research Center for Nuclear Physics, Osaka University, Ibaraki, Osaka 567-0047, Japan.

‖Also associated with PNPI, St. Petersburg, Russia.

data. Analyzing powers for $\pi^\pm$ production by a polarized antiproton beam have the same magnitude, but opposite sign [3]. Sizable values of A_N for inclusive π^+ production by polarized protons were also observed at 11.75 GeV/c [4]. Measurements of the inclusive production of π^0 and η^0 were also made at 200 GeV/c as functions of x_F [5–7], and these are shown in Fig. 1 as well.

In addition to pion asymmetries, large effects were observed for the transverse polarization P_N of several hyperons from unpolarized beams and targets [8]. In hyperon production, the magnitude of P_N seems to be independent of energy over fixed-target (equivalent) energies from 12 GeV to 2000 GeV. It is only slightly smaller for nuclear targets compared to hydrogen, which has been explained as a rescattering effect [8]. There is some reason to believe that the asymmetries in meson production and the polarization in hyperon production are related (i.e. they are both significant only in the beam fragmentation region and they depend on the flavor quantum numbers of the produced particle) [9,10]. Therefore, based on the E704 results, it is reasonable to expect sizable asymmetries in pion inclusive production over a wide energy range.

The Relativisitic Heavy Ion Collider (RHIC) at Brookhaven National Laboratory will offer an exciting opportunity to collide polarized proton beams at energies up to $\sqrt{s}=500$ GeV and luminosities up to 2×10^{32} /cm^2 sec. The accessible physics will include the study of the spin content of the proton, particularly gluon and antiquark polarization, the study of large perturbative QCD-predicted asymmetries for parton-parton subprocesses, and searches for parity violation [11]. An achievable goal for beam polarization at RHIC is expected to be about 70%, and it will have to be measured in a range spanning from the injection momentum of about 24 GeV/c up to 250 GeV/c.

The analyzing power A_N of inclusive pion production by polarized protons is a prime candidate for use in high energy proton polarimetry, where A_N is defined as

$$A_N=\frac{1}{P_b}\left[\frac{n_+-n_-}{n_++n_-}\right], \tag{1.1}$$

and P_b is the beam polarization. The $n_\pm$ are event rates for the positive and negative beam spin states, respectively, when the pion or proton is produced to the left of the beam if + beam spin is upward. If there are symmetric left and right detectors, a different expression can be used that is less sensitive to systematic effects; see Sec. III.

In this paper results are presented of measurements of analyzing powers for the inclusive reactions $p_\uparrow p\rightarrow\pi^\pm X$, $p_\uparrow C\rightarrow\pi^\pm X$, and $p_\uparrow C\rightarrow pX$. Data were also collected with polarized proton beams on a CH_2 target, providing a check of the results on carbon and hydrogen. Measurements of scattering off a carbon target were made in November 1997, and off a liquid hydrogen target in March 1999, using a transversely polarized 22-GeV/c proton beam extracted from the Brookhaven Alternating Gradient Synchrotron (AGS). The kinematic range covered by the experiment was transverse momentum p_T from 0.3 to 1.2 GeV/c, and x_F from 0.45 to 0.8. The main purpose of the experiment was to measure A_N for inclusive charged pion production at 22 GeV/c at similar kinematics to the 200 GeV/c results. A secondary goal was to provide a comparison of the pion asymmetries from production on hydrogen and carbon targets. The final goal was to determine the feasibility of using pion inclusive polarimetry for RHIC or the DESY ep collider HERA polarized beams. Carbon was used in addition to liquid hydrogen (as in E704) because a thin carbon target was planned to be used for the RHIC polarimeter. This experiment tested both the energy and target dependence of inclusive pion production. The results are also compared with data from other experiments performed at higher and lower energies [2,4].

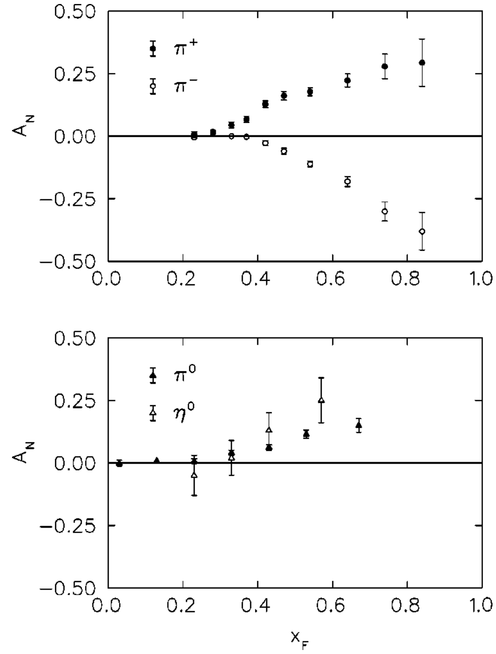

FIG. 1. Analyzing powers A_N vs x_F from the E704 experiment at Fermilab. The incident momentum of the polarized proton beam for E704 was 200 GeV/c. The p_T- acceptance ranges for $\pi^\pm$, π^0, and η^0 were 0.2 to 2.0, 0.5 to 2.0, and 0.7 to 2.0 GeV/c, respectively. (a) π^+ and π^- data. (b) π^0 and η^0 results.

The polarized beam and the AGS polarimeter are described in Sec. II and the Appendix. The experiment consisted of two parts, a local absolute polarimeter (Sec. III) and the magnetic spectrometer to detect the inclusively produced charged particles (Sec. IV). The inclusive data-analysis details and results are given in Sec. V, the interpretation in Sec. VI, and conclusions in Sec. VII. Results with the carbon target were published in Ref. [12].

II. THE POLARIZED PROTON BEAM

An earlier, comprehensive description of the AGS polarized proton beam acceleration and polarimetry is given in Ref. [13]. Significant improvements since then involve the addition of a booster ring and new techniques to handle spin resonances. The latter include a partial Siberian Snake [14,15] to overcome imperfection resonances, and a radio frequency (rf) dipole [16–18] to overcome intrinsic resonances. The rate capability and performance of the AGS internal polarimeter were also improved.

The polarized beam originated with an atomic beam type H^- ion source which produced typically a current of 25 μA over a 250 μsec long pulse at 20 keV. The beam was then accelerated to 760 keV using a radio frequency quadrupole (RFQ), and then to 200-MeV kinetic energy using the linear accelerator (LINAC). At this point, the beam polarization could be measured in a separate branch of the beam line using the reaction $p+C\rightarrow p+X$ at the two laboratory scattering angles of 12° and 16°. Polarization was typically 77%, with a 1% statistical accuracy attained in a few minutes. The booster accelerated the beam to 1.5 GeV with little to no polarization loss and delivered the beam to the AGS.

The circulating AGS polarized proton beam, which had an intensity of a few 10^9 protons in one rf bunch, was then accelerated to a momentum of 22 GeV/c. Acceleration and preservation of the beam polarization is described in Refs. [15,17,18]. Both for polarization measurement and extraction to the experiment, the beam was debunched with approximately a 1 sec "flat top" (of the AGS magnet currents). Measurement of beam polarization with the internal AGS polarimeter used pp elastic scattering at $t\simeq -0.15$ GeV$^2/c^2$ by observing the recoil proton. These measurements were performed, as required, for polarization optimization and monitoring. A 1.5% statistical accuracy was obtained in 15 min at top energy. (This polarimeter is described in the Appendix.)

Resonant extraction to wire and Lambertson septa delivered the beam to the switchyard [19] and into the external B-B1 beam line. Calculations of the external beam optics were done using TRANSPORT code to optimize the beam size and divergence at the B (fixed hole) and B1 (vertical) collimators where the beam intensity was reduced from 3×10^9 to approximately 1×10^8. The beam emittance was then calculated after collimation and the TRANSPORT code was again used to set the magnetic elements to define the beam spot σ_x,σ_y (1.5 mm, 2.5 mm) and divergence σ_x',σ_y' (2.5 mrad, 1.4 mrad) at the experimental target. The beam momentum dispersion at the target was set to zero. The intensity and momentum acceptance were further reduced and controlled by a variable horizontal collimator to $(3-4)\times10^7$ protons per pulse at the experiment. The calculated B1 beam envelope and dispersion are shown in Fig. 2. The beam intensity, position, and size at the experiment were monitored using ion chambers and segmented wire ion chambers (SWICs) at three locations.

The spin transport [20] from the AGS through the B-B1 lines to the experiment was also calculated. The directional cosine of the stable spin direction at the target was determined to be 0.99 from vertical. The beam intensity reduction by the collimators could lead to a different polarization of the selected beam versus that measured in the AGS. However, an external polarimeter, using the pp elastic-scattering reaction, at the experiment continuously monitored the beam polarization and was used to normalize the data.

The sign of the beam polarization for each AGS spill originated at the polarized proton source controls, and it was latched into a flip-flop in the experimental logic using the

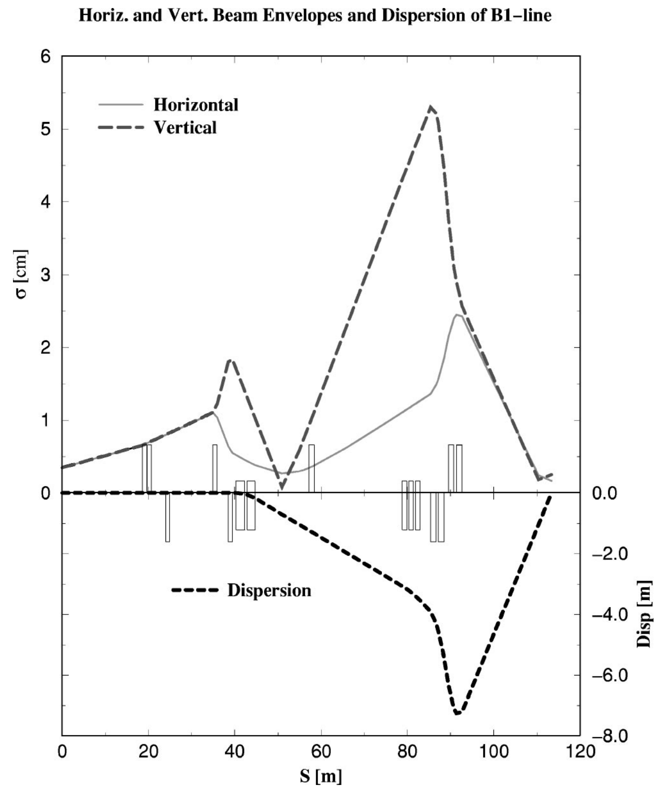

FIG. 2. Plot of the computed beam envelope and dispersion as a function of position along the B1 beam.

signal corresponding to the beginning of the AGS spill. The flip-flop outputs were latched and read out for every event, and they also gated some of the scalers, which were read out every spill. These two methods for recording the polarization direction (latched information for each event and gated scalers for every spill) allowed a cross check—events and scalers that disagreed within a spill were discarded from further analysis.

III. PROTON-PROTON ELASTIC POLARIMETER: MEASUREMENT OF THE BEAM POLARIZATION

The absolute beam polarization was determined locally using the pp elastic-scattering reaction at Mandelstam t of $-(0.15\pm0.05)$ (GeV/c)^2. The analyzing power has been measured [21] to an accuracy of $\pm12\%$. A top view of the layout of all the counters in the horizontal plane is sketched in Fig. 3. The asymmetry of pp elastic scattering and the asymmetries of inclusive processes were measured simultaneously by two independent sets of counters, targets, electronics, and data acquisition systems.

A. Elastic experimental setup

The kinematic region for pp elastic scattering of $-t=0.15\pm0.05$ (GeV/c)^2 was chosen because it gave a large cross section and asymmetry according to a previous measurement [21]. In order to detect both the forward and backward (recoil) protons, a forward acceptance of 0.80° to 1.2° and a backward acceptance of $76°-80°$ was required in laboratory scattering angles.

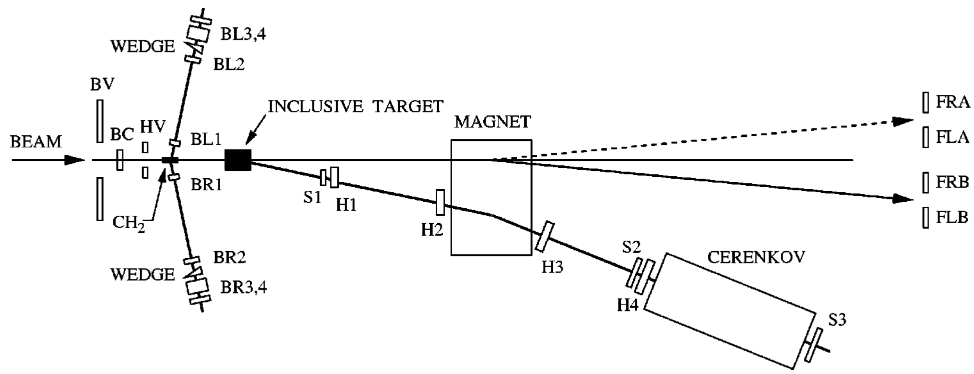

FIG. 3. Schematic of the experimental layout (not to scale). The elastic scattering detectors included BL1-BL4, BR1-BR4, FLA, FLB, FRA, and FRB. The magnetic spectrometer for the inclusively produced particles included trigger scintillators S1–S3 and hodoscopes H1–H4. The position of the carbon target is shown; the liquid hydrogen target center was located about 17 cm downstream of this position when it was installed. The luminosity counter telescopes viewing the inclusive target above and below the beam are not shown for clarity.

The two arms of the elastic polarimeter, which each consisted of four backward (B1, B2, B3, B4—designated BR1, BR2, . . . , BL3, BL4) and two forward or F counters, are shown in Fig. 3. All of these counters were made of plastic scintillator with either one or two (on the B2 counters only—denoted BR2U, BR2D, BL2U, BL2D) Hamamatsu H1161-50 photomultiplier tubes. Dimensions and positions of the counters are given in Table I. Start signals from the B1 counters and stop signals from B2, B3, and F counters went to individual time-to-digital converter (TDC) channels, thereby giving time of flight information. The B1 to B2 flight times for elastic recoil protons were in the range 7.0–8.0 ns, whereas the flight time of a particle with $\beta=1$ was 3.1 ns. Consequently, 1-ns timing resolution was required to make the time of flight measurement useful. The kinetic energy of the recoil protons varied considerably as a function of scattering angle. Thus, wedge-shaped aluminum absorbers were placed between the B2 and B3 counters on both arms in order to equalize the proton kinetic energies arriving at the B3 counters. The thickness of the B3 counters was chosen to stop recoiling elastic protons, whereas other particles passed through and were detected by the B4 counters. The B4 counters thus served as veto counters for elastic events. Forward elastic protons were detected by the F counters in coincidence with the B counters. For each arm, two sets of forward counters (FRA, FLA and FRB, FLB) were needed due to the fact that the beam and the forward elastic protons were bent by the analyzing magnet of the pion inclusive spectrometer. The bend was either to the left or to the right of the nominal beamline, depending on whether the magnet polarity setting was "A" (for π^-) or "B" (for π^+, p) in the

TABLE I. Positions and dimensions of elastic polarimeter and inclusive counters. The hodoscope thicknesses correspond to a single counter for H1 and H2, and to a pair of counters for H3 and H4 (which had both x and y planes). However, half the area of each hodoscope plane had double the recorded thickness due to overlap of neighboring counters. The dimensions of the S1 and S2 counters are approximate.

Name	Size ($h\times w\times d$) (mm^3)	Position from the target
B1	20×15×1	8 cm, 78°
B2	70×80×2	102 cm, 78°
B3	70×80×45	114 cm, 78°
B4	80×100×10	116 cm, 78°
F	10×60×10	~11 m, ~0.96°
S1	60×60×6	137 cm
H1	66×66×3	152 cm
H2	66×66×3	315 cm
H3	98×98×6	662 cm
S2	105×105×6	810 cm
H4	114×114×6	825 cm
S3	203×203×6	~11 m

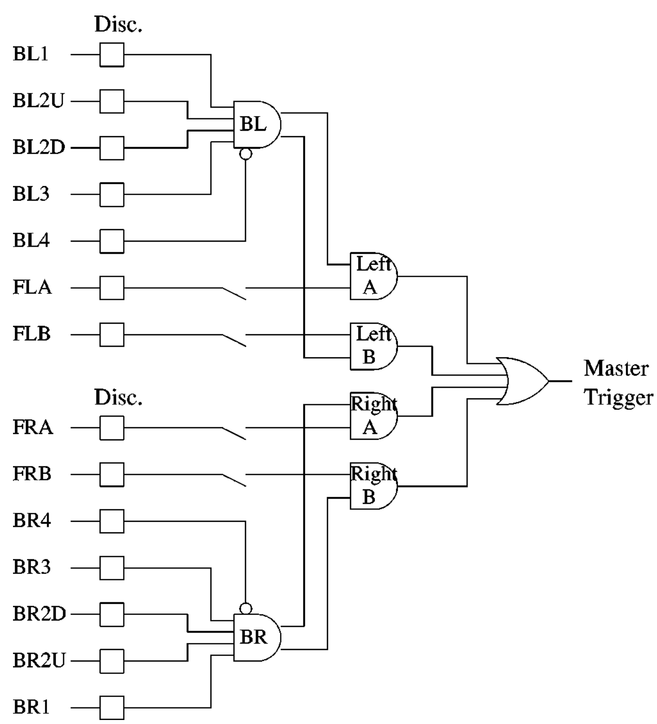

FIG. 4. Trigger logic diagram of the pp elastic polarimeter.

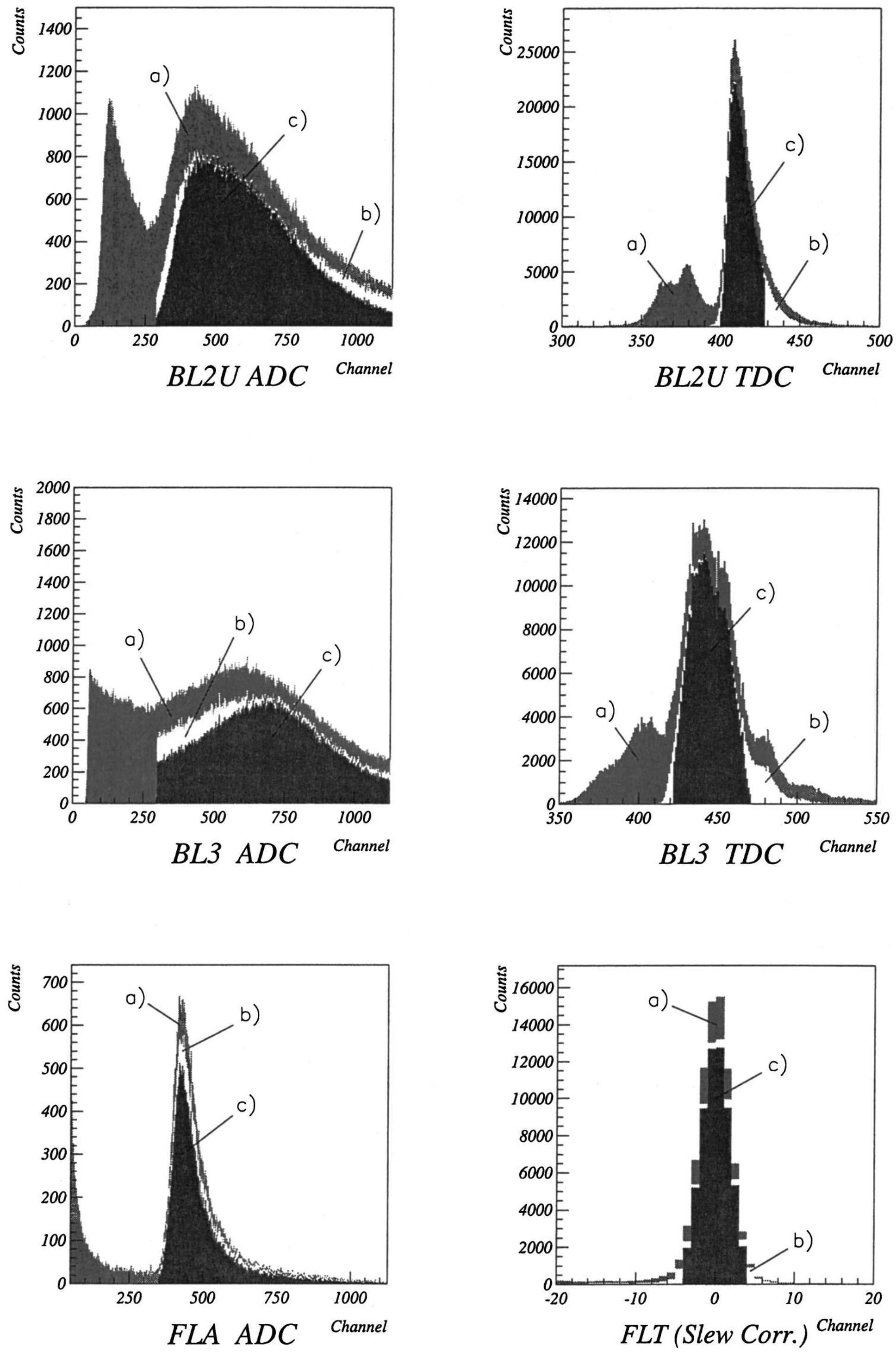

FIG. 5. Effects of cuts on ADC and TDC distributions. For each quantity, region *a* (gray) gives the raw distribution, region *b* (white) shows events remaining after ADC cuts on all counters, and region *c* (black) corresponds to the selected elastic candidate events after the final TDC cut on the forward counter. The timing resolution was 0.1 ns per TDC channel. FLT is the corrected value for the FLA TDC data.

magnet control system (see Fig. 3). The magnet delivered a momentum kick of approximately 1 GeV/c.

A CH_2 target of (width$\times$height$\times$length) dimensions $5\times30\times15$ mm^3 was oriented edge-on to the beam. For doing systematics studies of the carbon background, a graphite block of dimensions $2\times30\times15$ mm^3 was used in place of the CH_2.

Figure 4 shows the trigger logic diagram for the elastic polarimeter. Signals from the forward counters were included in the coincidences at times. However, data were usually collected with the trigger on the backward arms alone, so that the recoil asymmetries could be measured. Thus, the forward counters were not normally in the trigger. The final beam polarization results required a forward-backward arm coincidence, either in hardware or software. The trigger signal caused the logic to latch until the data were read by the computer. A CAMAC (computer automated measurement and control) output register was used to provide a ‘‘computer done’’ signal to unlatch the logic. The interrupt latency varied from 20 μs to a few hundred μs.

The data-acquisition (DAQ) system for the *pp* elastic polarimeter was entirely separate from that of the pion inclusive setup, but was quite similar to it. A personal computer with a 120-MHz Cyrix processor, a proprietary CAMAC crate controller made by DSP, a DSP computer interface card, and an interconnecting cable formed each DAQ system. Only one CAMAC crate could be read per personal computer, but this was sufficient for the experiment. For example, analog-to-digital converter (ADC) and TDC data were recorded for all elastic counters. Three kinds of interrupts to the DAQ computers were employed, one for the beginning of the AGS spill, one for events, and one for the end of the spill.

The DAQ software ran in the DOS 6.20 operating system, and was largely written in the Microsoft QUICKBASIC language, which included some built-in functions for accessing the computer input/output ports. Included in the DAQ program was a processor of lists of CAMAC functions and asymmetry calculations; user-modifiable routines for setup, begin spill, event processing, end spill, and end run; and linked libraries for CAMAC commands and for histogram display graphics. Simple analysis tasks, such as accumulating polarization-tagged scaler sums or filling of histograms, were done between spills. For the elastic scattering part of this experiment, pulse heights and flight times for the counters were histogrammed. At the end of the run, scaler ratios and spin asymmetries were calculated to monitor hardware performance.

During a spill, all the events were stored in memory ($\sim$2 ms/event) and were then written to disk between spills. As a result, dead time was greatly reduced. For the November 1997 runs, the events were stored in RAMDISK. It was found that the DAQ system rate at high beam intensity was limited by the time to transfer the data from RAMDISK to disk between spills. If the event rate was too high, the time to copy the data became too long and entire spills were lost. Thus, the elastic DAQ rate was limited to less than 140 and the inclusive rate to less than 400 events per spill. Such a problem only occurred during one run period (P3–see below) for the elastic part of the experiment. For the March 1999 runs, the events were written to an array in RAM during each spill. Because of the array sizes allowed within DOS and the QUICKBASIC language, the elastic and inclusive rates were then limited to 400 and 700 events per spill, respectively. These were more than the trigger rates, and the dead times were generally less than 20% at a beam intensity of 3×10^7 per spill.

B. Elastic polarimeter data analysis and results

1. Run period selection

Because the goal of the elastic polarimeter was to measure the beam polarization during the same time period when the inclusive pion production measurements were being carried out, only those data were used when both the elastic and inclusive parts of the experiment were running simultaneously. Individual CH_2 elastic target runs were grouped into three time periods, denoted P1, P2, and P3 during the runs with the carbon inclusive target (1997), and periods P4–P7 during the hydrogen inclusive target runs (1999). A series of carbon target and empty target systematics runs were performed between P1 and P2, again after P3, and during P7. It was realized at the end of period P2 that the beam had not been properly centered horizontally on the elastic polarimeter target, which affected the trigger rate, but the beam was correctly positioned from P3 onward. The inclusive spectrometer was not affected by the change in beam position because the dimensions of the inclusive carbon target (located downstream of the elastic target) were larger than the beam spot both horizontally and vertically. Within the time periods there were changes in the polarity of the inclusive spectrometer’s analyzing magnet. Accordingly, the seven main periods were further subdivided into 12 periods, denoted P1A, P1B, P2B, P3A, P3B and P4A, P4B, P5A, P5B, P6A, P6B, P7A, where A and B refer to the magnet polarity. However, a few runs were taken with the magnet at B polarity during period P7A.

2. Elastic event selection

Prior to applying cuts designed to isolate *pp* elastic-scattering events, a correction was made to the TDC information of the forward counters. This slewing effect occured because the raw signal pulses were fed into constant-threshold discriminators before the TDCs. To correct for this, the strong correlation of ADC and TDC data was fit with a function of the form

$$(\mathrm{TDC})_{fit} = (\mathrm{TDC})_{data} C_1 + \frac{C_2}{\sqrt{\mathrm{ADC}}}. \tag{3.1}$$

The quantity $(\Delta)^2 = [(\mathrm{TDC})_{data} - (\mathrm{TDC})_{fit}]^2$ was minimized with respect to parameters C_1 and C_2. The resulting distribution of Δ had a symmetric Gaussian shape.

The cuts applied to the raw data to isolate the *pp* elastic signal were threefold.

(1) Events were selected for which all counters of one arm had non-overflowing TDC information. The uppermost (gray) traces in the first four panels in Fig. 5 show the resulting raw ADC and TDC spectra for the ‘‘left’’ arm. (Note the early peak in the BL2U TDC spectrum, was produced by relativistic particles, which either scattered in BL3 or failed to penetrate to veto counter BL4.)

(2) Threshold cuts were applied to the ADC spectra of all counters in the arm. The ADC and TDC spectra of the middle traces (white) in Fig. 5 are shown for events which passed the ADC threshold cut in all counters of the ‘‘left’’ arm. The cut on BL3, in particular, also eliminated some elastic scattering events. Such losses may have been different for the left and right arms. However, no difference in the asymmetry (within a fraction of a standard deviation) was observed with or without such a tight cut.

(3) In the forward counters only, the peaks in the TDC spectra of the surviving (slewing-corrected) events were fit with a Gaussian, and events outside of 2 standard deviations (σ) from the mean were rejected. The spectra for events which passed this restriction for all counters of the "left" arm are the lowest (black) of the three traces in Fig. 5. Studies of varying the TDC cuts from 1σ to 3σ showed no significant difference in the resulting asymmetries.

3. Background estimation

Comparisons of rates from carbon target and empty target runs with normal CH_2 target runs yielded the following background estimates.

Carbon contribution to events in the backward arms: 40–60 %.

Carbon contribution to forward/backward coincidences: 2–4 % in 1997 and $(7.0\pm0.3)\%$ in 1999.

Non-target contribution to events in the backward arms: 1–5 %.

Non-target contribution to forward/backward coincidences: $<0.3\%$.

The total contribution to events which survive the cuts previously described, including contributions from processes other than *pp* elastic scattering, is estimated to be 3–5 %. Corrections to the raw asymmetry due to the presence of background are discussed below.

4. Raw asymmetries

Raw asymmetries were calculated from the measured counts:

$$\begin{aligned} N_L^{\uparrow} &= I_0 B^{\uparrow} d\Omega_L (1+P_b^{\uparrow} A_{NL}) \\ N_L^{\downarrow} &= I_0 B^{\downarrow} d\Omega_L (1-P_b^{\downarrow} A_{NL}) \\ N_R^{\uparrow} &= I_0 B^{\uparrow} d\Omega_R (1-P_b^{\uparrow} A_{NR}) \\ N_R^{\downarrow} &= I_0 B^{\downarrow} d\Omega_R (1+P_b^{\downarrow} A_{NR}), \end{aligned}$$

where N_L is the number of events detected by the left forward and right recoil arms, and similarly for N_R. The superscripts $\uparrow$ and $\downarrow$ indicate polarization states up and down. The integrated beam intensities are $B^{\uparrow}$ and $B^{\downarrow}$, and the average beam polarizations are $P_b^{\uparrow}$ and $P_b^{\downarrow}$ for these two polarization states. Similarly, the effective solid angles times efficiencies are $d\Omega_L$ and $d\Omega_R$, and the analyzing powers are A_{NL} and A_{NR} for the two sets of counters. A normalization, I_0, includes target thickness and other constant factors. Then, the raw asymmetries ϵ were computed using the formula

$$\begin{aligned} \epsilon &= \frac{\sqrt{N_L^{\uparrow}\times N_R^{\downarrow}}-\sqrt{N_L^{\downarrow}\times N_R^{\uparrow}}}{\sqrt{N_L^{\uparrow}\times N_R^{\downarrow}}+\sqrt{N_L^{\downarrow}\times N_R^{\uparrow}}} \\ &\approx P_b A_N + P_b^2 A_N^2(\epsilon_P^2+\epsilon_A^2)+\text{h.o.t.}, \end{aligned} \tag{3.2}$$

which is accurate up to higher order terms (h.o.t.) in the small quantities $P_b A_N$, ϵ_P, and ϵ_A (ϵ_B and ϵ_Ω below are also presumed to be small). The statistical error is given by

$$\sigma_\epsilon = \frac{1}{L+R}\left(\frac{LR}{L+R}\right)\sqrt{\frac{1}{N_L^{\uparrow}}+\frac{1}{N_R^{\downarrow}}+\frac{1}{N_R^{\uparrow}}+\frac{1}{N_L^{\downarrow}}}, \tag{3.3}$$

where $L\equiv\sqrt{N_L^{\uparrow}\times N_R^{\downarrow}}$ and $R\equiv\sqrt{N_L^{\downarrow}\times N_R^{\uparrow}}$. In these expressions, the mean beam polarization and analyzing power and their respective asymmetries are

$$\begin{aligned} P_b &= (P_b^{\uparrow}+P_b^{\downarrow})/2 \\ A_N &= (A_{NL}+A_{NR})/2 \\ \epsilon_P &= \frac{P_b^{\uparrow}-P_b^{\downarrow}}{P_b^{\uparrow}+P_b^{\downarrow}} \\ \epsilon_A &= \frac{A_{NL}-A_{NR}}{A_{NL}+A_{NR}}. \end{aligned}$$

Equation (3.2) holds provided the acceptances and efficiencies of the left and right arms remained constant during the measurement of both beam states. Flipping the beam polarization with every spill ensures that any slow changes in counter efficiencies tend to cancel out. However, an intensity dependence in counter efficiency can affect the spin asymmetry if the intensities of pulses arriving at the target are systematically different for the two beam states. A cross-check of the asymmetry in beam intensity ϵ_B can be calculated from the formula [22]

$$\begin{aligned} \alpha_{11} &= \frac{\sqrt{N_L^{\uparrow}\times N_R^{\uparrow}}-\sqrt{N_L^{\downarrow}\times N_R^{\downarrow}}}{\sqrt{N_L^{\uparrow}\times N_R^{\uparrow}}+\sqrt{N_L^{\downarrow}\times N_R^{\downarrow}}} \\ &\approx \epsilon_B + P_b A_N \epsilon_A + \text{h.o.t.} \\ &\approx \epsilon_B = \frac{B^{\uparrow}-B^{\downarrow}}{B^{\uparrow}+B^{\downarrow}}. \end{aligned} \tag{3.4}$$

A nonzero ϵ_A can come about through misalignment of left and right arms and a strongly angle-dependent analyzing power A_N. As long as the magnitude of ϵ_B was less than 0.1, there would be a negligible effect on the polarization asymmetry in Eq. (3.2) for this experiment.

The asymmetry in the unpolarized differential cross section integrated over the acceptances and efficiencies of the left and right arms, ϵ_Ω, can be calculated from the formula [22]:

$$\begin{aligned} \alpha_{10} &= \frac{\sqrt{N_L^{\uparrow}\times N_L^{\downarrow}}-\sqrt{N_R^{\uparrow}\times N_R^{\downarrow}}}{\sqrt{N_L^{\uparrow}\times N_L^{\downarrow}}+\sqrt{N_R^{\uparrow}\times N_R^{\downarrow}}} \\ &\approx \epsilon_\Omega + P_b A_N \epsilon_P + \text{h.o.t.} \\ &\approx \epsilon_\Omega = \frac{d\Omega_L - d\Omega_R}{d\Omega_L + d\Omega_R}. \end{aligned} \tag{3.5}$$

The assumption that ϵ_P is small is generally made universally. In any case, it cannot easily be checked without comparing rates directly to a beam polarization state which is

TABLE II. Various asymmetries by the running period from elastic polarimeter events with forward/recoil coincidences.

Period	ϵ	$\alpha_{11} \simeq \epsilon_B$	$\alpha_{10} \simeq \epsilon_\Omega$
P1A	0.0152 ± 0.0119	0.0152 ± 0.0119	0.1799 ± 0.0115
P1B	0.0224 ± 0.0063	0.0077 ± 0.0063	0.2240 ± 0.0060
P2B	0.0112 ± 0.0052	-0.0092 ± 0.0052	0.1820 ± 0.0051
P3B	0.0110 ± 0.0129	0.0195 ± 0.0129	0.0505 ± 0.0128
P3A	0.0076 ± 0.0029	-0.0001 ± 0.0029	0.0238 ± 0.0029
P4B	0.0140 ± 0.0029	-0.0046 ± 0.0029	-0.0473 ± 0.0029
P4A	0.0201 ± 0.0028	0.0048 ± 0.0028	-0.0765 ± 0.0028
P5B	0.0065 ± 0.0066	0.0015 ± 0.0066	-0.0775 ± 0.0066
P5A	0.0194 ± 0.0034	0.0033 ± 0.0034	-0.0115 ± 0.0034
P6B	0.0089 ± 0.0047	-0.0083 ± 0.0047	0.0175 ± 0.0047
P6A	0.0154 ± 0.0031	-0.0010 ± 0.0031	0.0063 ± 0.0031
P7A	0.0184 ± 0.0025	-0.0023 ± 0.0025	0.0137 ± 0.0025
P1–P3			
Total	0.0107 ± 0.0023	0.0000 ± 0.0023	0.0878 ± 0.0022
Carbon	0.0841 ± 0.0449	0.0643 ± 0.0450	0.0195 ± 0.0452
P4–P7			
Total	0.0165 ± 0.0012	-0.0007 ± 0.0012	-0.0218 ± 0.0012
Carbon	-0.0099 ± 0.0333	0.0802 ± 0.0333	0.0407 ± 0.0333

known to be zero, as was done in one instance recently at Saclay [23]. A nonzero value of ϵ_Ω is not catastrophic, and in practice a value of 0.1 or less indicates reasonably good alignment of the left and right arms for a symmetric polarimeter.

The observed values for ϵ, α_{10}, and α_{11} are given for forward-backward coincidences in Table II, and for the backward arms only in Table III. Note that the left/right labeling of the actual counter names (see Fig. 3) was in the opposite sense from the usual convention. Ordinarily the ‘‘right’’ arm has its forward arm to beam right. The quoted asymmetries adhere to the standard left/right conventions rather than the one corresponding to the labeling of the counters. No evidence for a nonzero ϵ_B was observed, and the effect of centering the beam on the elastic target (and thereby improving the alignment) between running periods P_2 and P_3 is clearly reflected in the already-small values of ϵ_Ω. The final raw asymmetry for the CH_2 target observed from forward/backward coincidences was

$$\epsilon_{CH_2} = 0.0107 \pm 0.0023 \quad (\mathrm{P1–P3})$$

$$= 0.0165 \pm 0.0012 \quad (\mathrm{P4–P7}).$$

These values were obtained from the event totals integrated over the respective running periods.

5. Effect of carbon contamination

Ordinarily carbon contributions from ϵ_{CH_2} should be subtracted in order to extract the elastic *pp* asymmetry, ϵ_{pp}. However, the carbon data were not used because of the following.

The statistical significance was small. The measured carbon asymmetry (ϵ_C) did not differ by more than 2σ from zero during periods P1–P3 or P7. Thus, the statistics of the carbon results were not good enough to correct the CH_2 data.

No carbon data were taken for the B polarity of the inclusive analyzing magnet during either the carbon or hydrogen inclusive measurements.

The *p*-carbon analyzing power is known to be smaller (by about a factor of two) than the *pp* analyzing power from asymmetry measurements done with the E880 polarimeter internal to the AGS ring. Experiment E880 was running at the same beam energy concurrently with the experiment described here, in order to monitor the time stability of the beam polarization [14,16] in the AGS; see the Appendix.

The carbon-target asymmetry data indicated (with limited statistics) that the carbon analyzing power is small. Furthermore, although there are no data points available at this energy, the carbon analyzing power is smaller than that for *pp* at $p_{lab} \leqslant 3.5$ GeV/c [24,25], and at $p_{lab} = 185$ GeV/c [26].

Two cases were therefore considered:

(1) $A_C = A_{CH_2}$

(2) $A_C = 0$.

In the presence of carbon background, the asymmetry for the *pp* elastic part is given by

$$\epsilon_{pp} = \frac{\epsilon_{CH_2} - n_C \times \epsilon_C}{n_p}, \tag{3.6}$$

where n_p is the fraction of the total number of CH_2 target events contributed by *pp* elastic scattering, and n_C is the fraction from *p*C. By definition, $n_p + n_C \equiv 1$. The uncertainty in ϵ_{pp} is given by

TABLE III. Same as Table II, but using data from the backward arm only.

Period	ϵ	$\alpha_{11} \simeq \epsilon_B$	$\alpha_{10} \simeq \epsilon_\Omega$
P1A	0.0121 ± 0.0050	-0.0035 ± 0.0050	0.1043 ± 0.0049
P1B	0.0111 ± 0.0025	0.0044 ± 0.0025	0.1094 ± 0.0025
P2B	0.0081 ± 0.0020	-0.0019 ± 0.0020	0.0945 ± 0.0020
P3B	0.0095 ± 0.0051	0.0067 ± 0.0051	0.0392 ± 0.0051
P3A	0.0090 ± 0.0012	-0.0008 ± 0.0012	0.0467 ± 0.0012
P4B	0.0121 ± 0.0013	-0.0038 ± 0.0013	-0.0529 ± 0.0013
P4A	0.0130 ± 0.0011	0.0038 ± 0.0011	-0.0635 ± 0.0011
P5B	0.0098 ± 0.0027	0.0103 ± 0.0027	-0.1660 ± 0.0027
P5A	0.0136 ± 0.0015	0.0037 ± 0.0015	-0.0239 ± 0.0015
P6B	0.0065 ± 0.0021	-0.0017 ± 0.0021	-0.0275 ± 0.0021
P6A	0.0107 ± 0.0013	-0.0033 ± 0.0013	-0.0305 ± 0.0013
P7A	0.0111 ± 0.0010	-0.0020 ± 0.0010	-0.0283 ± 0.0010
P1–P3			
Total	0.0092 ± 0.0009	-0.0002 ± 0.0009	0.0667 ± 0.0009
Carbon	0.0030 ± 0.0052	0.0080 ± 0.0052	0.0205 ± 0.0052
P4–P7			
Total	0.0116 ± 0.0005	-0.0001 ± 0.0005	-0.0445 ± 0.0005
Carbon	0.0011 ± 0.0037	-0.0044 ± 0.0037	-0.0281 ± 0.0037

$$(\Delta \epsilon_{pp})^2 = \left(\frac{\Delta \epsilon_{CH_2}}{n_p} \right)^2 + (\epsilon_C - \epsilon_{CH_2})^2 \left(\frac{\Delta n_p}{n_p^2} \right)^2 + \left(1 - \frac{1}{n_p} \right)^2 (\Delta \epsilon_C)^2. \tag{3.7}$$

Using $n_p = 0.97 \pm 0.01$ and 0.930 ± 0.003 during the carbon and hydrogen target inclusive data, respectively, the results for the two cases above (given for periods P1–P3 and P4–P7) are

$A_C = A_{CH_2}$: $\epsilon_{pp} = 0.0107 \pm 0.0023$, 0.0165 ± 0.0012
$A_C = 0$: $\epsilon_{pp} = 0.0110 \pm 0.0026$, 0.0177 ± 0.0013.

For the final results, the mean values were taken:

$$\begin{aligned} \epsilon_{pp} &= 0.0108 \pm 0.0024 \text{ (stat)} \\ &\quad \pm 0.0003 \text{ (syst)} \quad \text{(P1–P3)} \\ &= 0.0171 \pm 0.0013 \text{ (stat)} \\ &\quad \pm 0.0006 \text{ (syst)} \quad \text{(P4–P7)}. \end{aligned}$$

The statistical error (stat) comes from the first term of Eq. (3.7), and the systematic error (syst) comes from the quadratic sum of the second and the third term of equation (3.7) or represents half the difference between the results of the two cases, whichever is larger. The systematic error depends on the value of A_C.

6. Beam polarization

The value of the analyzing power used to determine the beam polarization (at $p_{lab} = 22$ GeV/c and $t = -0.15$ (GeV/c)^2) was $A_N = 0.040 \pm 0.0048$. This value was determined from a phenomenological analysis of existing data, especially measurements from 10–45 GeV/c [21,27,28]. The quoted uncertainty was estimated from the 24 GeV/c results of Ref. [21], including both statistical and systematic errors. The phenomenological analysis was inspired by the fit given in Ref. [22]. The beam polarization was thus found to be

$$\begin{aligned} P_b &= 0.271 \pm 0.059 \text{ (stat)} \\ &\quad \pm 0.033 \text{ (syst)} \quad \text{(P1–P3)} \\ &= 0.427 \pm 0.032 \text{ (stat)} \\ &\quad \pm 0.053 \text{ (syst)} \quad \text{(P4–P7)}. \end{aligned}$$

The systematic error above includes the total uncertainty from the pp elastic-scattering analyzing power.

IV. PION INCLUSIVE SPECTROMETER SETUP

A. Apparatus

An entirely separate scattering target and set of detectors were used to measure the inclusive pion and proton production (see Fig. 3). Two primary targets were used in different years. In 1997 a carbon target was located 21 cm downstream of the elastic-polarimeter target. It was a graphite block of dimensions 5.0 cm wide by 6.0 cm high by 4.0 cm thick. In 1999 a liquid hydrogen target replaced the carbon block and was centered 38 cm downstream of the elastic-polarimeter target. Its dimensions were 25 cm long with a diameter of 6.3 cm. We also parasitically looked at inclusive events coming from the elastic CH_2 target.

The spectrometer itself consisted of three scintillators S1, S2, and S3, four hodoscopes H1, H2, H3, and H4, a bending

TABLE IV. Positions of the beam luminosity counters. All counters were 1.5 cm square and 0.64 cm thick.

Counter	LU1	LU2	LU3	LD1	LD2	LD3
Angle 1997	$+16°$	$+16°$	$+16°$	$-16°$	$-16°$	$-16°$
Angle 1999	$+8°$	$+8°$	$+8°$	$-8°$	$-8°$	$-8°$
Distance from Target (cm)	53.3	66.0	78.7	53.3	66.0	78.7

magnet located between H2 and H3, and a Čerenkov detector for particle identification. Dimensions and positions of these counters and hodoscopes are given in Table I. The hodoscopes consisted of 6-mm-wide scintillators with 1/3 overlap between adjacent counters, thus forming arrays with 2-mm space segmentation [29,30]. Hodoscopes H1 and H2 consisted of 16 parallel counters each, oriented so as to measure horizontal (x) coordinates of charged tracks in 31 cells of 2 mm widths (the end cells were 4 mm wide). Hodoscope H3 had 24 counters in x and 24 more in y, and H4 consisted of 28 counters in both x and y. The analyzing magnet provided a p_T kick of about 1 GeV/c and could be reversed to select the charge of inclusive particles. In 1997 a soft iron plate of 8 mm thickness was placed on H3 between the photomultipliers and the analysis magnet to protect the tubes from the magnetic field. In 1999 the 8-mm-thick iron was replaced with 13-mm-thick iron, and 13-mm-thick iron shielding was added to H2 between the tubes and the magnet.

The Čerenkov counter was filled with CO_2 at a pressure of ~ 2 atm absolute pressure in 1997, corresponding to a pion threshold of 3 GeV/c as measured with a beam. The absolute pressure was ~ 3 atm in 1999.

Upstream of the center of the elastic target by 7.6 cm there was a group of four halo veto (HV) counters (HVU, HVD, HVL, HVR) consisting of overlapping scintillator slats arranged pairwise horizontally and vertically. Semicircular notches cut in the sides of each counter formed a circular aperture of diameter 2.5 cm, through which the beam passed en route to the scattering targets. Upstream of the halo veto counters there was a thin beam counter (BC) scintillator, and a beam profile monitor (SWIC) used for beam tuning. Finally, two additional large beam veto, or BV, counters (BVU, BVD) with semicircular notches forming a 12.7 cm diameter aperture were located 64.4 cm upstream of the elastic target to veto the outer portions of the beam halo.

Beam luminosity monitoring

Whereas the spin asymmetries from symmetric double-armed polarimeters can be extracted from raw counts in the arms using Eq. (3.2), single-armed experiments require the raw counts to be normalized by some spin-independent quantity which is proportional to the time-integrated beam flux seen by the target for each of the separate spin states. Two telescopes consisting of three colinear scintillators each were mounted in the vertical plane above and below the beam at a 16° laboratory angle in 1997 to serve this purpose. Having the telescopes in the plane of the polarization vector and at an angle corresponding to approximately 90° in the c.m. frame, where the analyzing power is zero, made these measurements less sensitive to polarization effects. In 1999 we were forced to change the angle to 8° because of interference from the support for the hydrogen target. (See Table IV for dimensions and positions of the counters. The luminosity counters are not shown in Fig. 3.) A logical OR of signals from three fold coincidences of the up and down arms (LOR) was scaled separately for the two beam spin states to provide the luminosity counts used for beam normalization when calculating inclusive asymmetries (see Fig. 6). The accidental coincidence rate was found to be $<0.5\%$.

In principle, the beam counter could also have been used for beam intensity monitoring; however, in practice it tended to be overwhelmed by the high rate from the beam (3×10^7 protons per 1.0 sec spill). In addition, the setup included an ion chamber located in the beam downstream of the analyzing magnet. Being in this position, the beam traversed the ion chamber at different angles depending on the magnet polarity. For this and other reasons the ion chamber was less stable as a beam monitor, and was therefore not used for asymmetry calculations.

B. Electronics and trigger logic

Figure 6 shows the inclusive trigger logic. Hits were required in S1, S2, and S3, and at least one counter in any three of the x planes of the four hodoscopes. In addition, Čerenkov counter signals were switched into the trigger for "π^+" running (B magnet polarity) and switched out for "proton" running (same magnet polarity). The Čerenkov counter was also out of the trigger for "π^-" running with the opposite (A) magnet polarity. At all times the master trigger was vetoed by separate OR's of the HV and BV counters. TDC and ADC information was recorded for S1, S2, S3, and the Čerenkov counter.

The data-acquisition system for the inclusive setup used similar hardware and software to that of the elastic polarimeter. Runs were usually started and stopped nearly simultaneously for both parts of the experiment in order to have data that closely corresponded to the same beam conditions. The inclusive-event rates varied from about 20 per spill for π^- running to over 200 per spill with the opposite beam polarity and the Čerenkov counter out of the trigger. Again, deadtime was minimal ($\sim 11\%$ in 1997 and $\sim 2\%$ in 1999) because events were stored in memory during the spill, and were written to disk between spills.

V. INCLUSIVE PARTICLE DATA ANALYSIS AND RESULTS

Inclusive data were collected at ~ 22 GeV/c (21.6 GeV/c during 1997 and 21.92 GeV/c in 1999) incident proton momentum in the three different running modes shown in Table V. During the first run (in 1997) we used only a carbon target and during the second run (in 1999) we used only a liquid hydrogen target.

The first step in data reduction was to look at the ratio of counts in the LOR luminosity scaler for the two beam spin states for each run. Out of a total of about 70 runs, two runs for which the LOR ratio differed by more than 0.02 from unity were discarded. Line 2 of Table VI shows the number

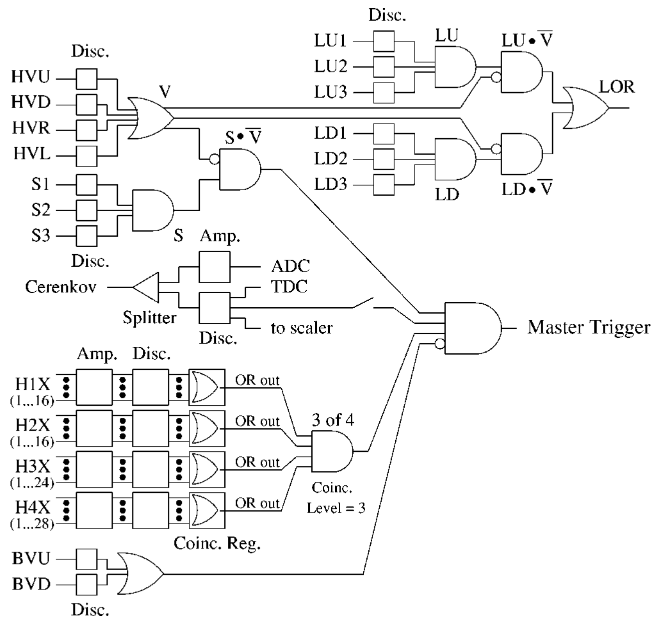

FIG. 6. Trigger logic diagram of the inclusive spectrometer and the beam flux monitor LOR. The individual counters of hodoscopes H1–H4 measuring the x positions are designated H1X, H2X, etc. The H3 and H4 counters measuring the y position were not used in the trigger.

of events which survived this step.

Events which passed all the cuts were binned in x_F and transverse momentum p_T. Feynman x_F is given for the inclusive reaction $a+b\rightarrow c+X$ by

$$x_F=\frac{p_L}{p_{max}}, \tag{5.1}$$

where p_L is the longitudinal momentum component of particle c in the center of mass frame and p_{max} is the maximum attainable center of mass momentum for any conceivable reaction which produces a particle of type c in the final state, given the known masses and momenta of particles a and b. The values of p_{max} were calculated using the formula [31]

$$p_{max}=\frac{\sqrt{\lambda}}{2\sqrt{s}}, \tag{5.2}$$

where the Mandelstam s and λ are given by

$$s=m_a^2+m_b^2+2m_bE_a \tag{5.3}$$

$$\lambda=s^2-2s(m_c^2-S_x)+(m_c^2+S_x)^2. \tag{5.4}$$

In the above, m_c is the mass of the inclusive particle and S_x is the square of the minimal invariant mass of the system X for a particular reaction. For 22-GeV/c incident protons, details about the calculation of p_{max} for inclusive π^-, π^+, and protons are given in Table VII.

TABLE V. Running modes for inclusive measurements.

Mode	Magnet polarity	Čerenkov in/out of trigger	Initial offline ADC cut
π^-	A	Out	(none)
π^+	B	In	>70
Proton	B	Out	<70

A. Track reconstruction method A

After decoding information from the hodoscopes, hit clusters in the hodoscopes were obtained. Each combination of hits in all four hodoscopes was fit by minimizing the quantity SX with respect to three parameters A_x, B_x, and a track momentum p. The definition of SX was given by

$$SX=\sum_{i=1}^{4}[x_i-f_i(z_i;A_x,B_x,p)]^2, \tag{5.5}$$

where x_i were the x positions of clusters in the four hodoscopes, z_i were the z positions of the four hodoscopes, and the f_i were functions of the form

$$f_i=B_x+A_xz_i+\frac{X(z_i)}{p}. \tag{5.6}$$

Using a model described in [32], the expression for $X(z)$ valid for purposes of fitting tracks through the inclusive spectrometer was

$$X(z)=\frac{Ke}{c}\int_{v=z_0}^{v=z}\int_{u=z_0}^{u=v}B_y(u)du\,dv, \tag{5.7}$$

where K is a constant, B_y is the y (vertical) component of the field map of the analyzing magnet field as a function of distance u along a particle track, and z_0 is the z coordinate of the starting point of the track. This expression assumes that the particle sees only a vertical field, and that the limited acceptances of the hodoscopes ensured that the path length through the analyzing magnet was essentially the same for all integration trajectories. The value of the constant K was found to be 1.013 from a Monte Carlo simulation of the experiment based on GEANT 3.21 [33]. Note that $B_y(u)$ was nonzero only for u in the region $z_2<u<z_3$. Taking $z_0=0$ and $z=z_i$, the expressions for f_i reduce to

$$f_1=B_x+A_xz_1 \tag{5.8}$$

$$f_2=B_x+A_xz_2 \tag{5.9}$$

$$f_3=B_x+A_xz_3+\frac{X_{23}}{p} \tag{5.10}$$

$$f_4=B_x+A_xz_4+\frac{X_{23}}{p}, \tag{5.11}$$

where

TABLE VI. The numbers of events surviving after applying miscellaneous analysis cuts for method A. This is for the carbon target. Details are in the text.

Criterion	A polarity	B polarity	
Total number of triggers	2.0×10^6	3.5×10^6	
	π^-	π^+	Proton
(1) Separation of B polarity into π^+,p by trigger type and initial Čerenkov ADC cut at channel 70	2.0×10^6	2.5×10^6	0.4×10^6
(2) After discarding runs with bad LOR ratio	1.96×10^6	2.48×10^6	0.4×10^6
(3) Number of "reconstructed" events ($SX_{min}<0.32$)	399634	1179679	269634
(4) Survive B_x cut ($-1.0\leqslant B_x\leqslant0.6$)	271009	889666	237980
(5) Survive S1/S3 ToF cut ($620\leqslant$TDC2$\leqslant840$)	257082	836895	231405
(6) Survive S1/Čerenkov ToF cut (π^-: no cut; π^+: $640\leqslant$TDC1$\leqslant840$; protons: TDC1$\geqslant2000$)	257082	836895	214502
(7) Survive Čerenkov ADC cut (for π^+ only, require ADC>200 for $x_F<0.6$, ADC>300 for $x_F>0.6$)	257082	448232	214502
(8) Survive hard cut on SX_{min} ($SX_{min}<0.05$).	225939	404469	199757
(9) Survive x_F, p_T cuts ($0.45<x_F<0.8, 0.3<p_T<1.2$)	218868	399024	192359

$$X_{23}=\frac{Ke}{c}\int_{v=z_2}^{v=z_3}\int_{u=z_2}^{u=v}B_y(u)\,du\,dv. \qquad (5.12)$$

Tests using the Monte Carlo simulation showed that the relative momentum uncertainty $\Delta p/p$ due to the tracking method was 2×10^{-3}, which was small compared to the momentum resolution of the experimental setup. (For example, the incident beam had a $\Delta p/p$ of about 4×10^{-3}.)

Tracks for which $SX_{min}\leqslant0.32$ cm^2 were considered "reconstructed." The requirement was deliberately left loose so that the background underneath the signal could be studied later in the analysis.

The trigger efficiency, defined as the ratio of the numbers in lines 3 and 2 of Table VI, was 20.4% for "π^-" mode, 47.5% for "π^+" mode, and 67.4% for "proton" mode. Because the trigger only required hits in three of the four hodoscopes, most of the events lost at this stage were ones for which there was no hit in one of the hodoscopes. The substantial differences in trigger efficiency were largely due to a combination of different physics processes contributing to the presence of a π^+, π^-, or proton being in the final state, differences in background levels, differences in trigger conditions, and the effects of pions decaying in flight.

The y-plane information from the hodoscopes was used to reduce background by requiring only one hit in each of H3 and H4. A projection was also made back to the target and a y cut was made.

TABLE VII. Values of p_{max} for the three running modes.

Inclusive particle	Reaction	s(GeV^2)	S_x	m_c	p_{max} (GeV/c)
π^-	$p+n\rightarrow p+p+\pi^-$	42.39	$(2m_p)^2$	m_π	2.974
π^+	$p+n\rightarrow n+n+\pi^+$	42.39	$(2m_n)^2$	m_π	2.982
p	$p+p\rightarrow p+p$	42.33	m_p^2	m_p	3.115

After reconstruction, a histogram of the B_x parameter for the tracks of runs from all three running modes is shown in Fig. 7. The B_x parameter was the x intercept of the track at the nominal target position of $z=0$. Owing to the geometry of the setup, increasingly negative B_x corresponds to the scattering vertex being further upstream in z. The distributions in Fig. 7 therefore show a large peak near zero coming from the carbon target, and a smaller one at more negative B_x coming from the CH_2 target of the elastic polarimeter further upstream. The fact that the center of the carbon-target peak is at about -0.5 cm rather than at zero indicates that the beam was hitting the carbon target slightly to the right of center in the nominal coordinate system. A cut of $-1.0\leqslant B_x\leqslant0.6$ selected tracks which had originated in the carbon target (see line 4 of Table VI).

Figure 8 shows a sampling of SX_{min} distributions from the tracking fits of events in three different x_F bins of the π^- data. Some background which increased with x_F remained in the sample at this stage. A hard cut rejecting events with $SX_{min}>0.05$ cm^2 was applied to all x_F bins of the data from all three running modes.

The x_F vs p_T distribution of all events, which passed the the hard cut on SX_{min} and additional ADC and TDC cuts described in Sec. V B, is shown in Fig. 9. A final cut outside the box $0.45\leqslant x_F\leqslant0.8$ and $0.3\leqslant p_T\leqslant1.2$ GeV/c was applied to all data to reject events with unphysical x_F or p_T values and events which appeared to have been outside the limits of the acceptance of the inclusive spectrometer. This cut concluded the raw-event selection phase of the data analysis. The total numbers of surviving events are given in line 9 of Table VI.

Background estimation

The plots of the SX_{min} distributions shown in Fig. 8 were produced from events which had passed all of the cuts in the event selection phase of the analysis. The background, which increased with x_F, is clearly visible. The remaining step in the analysis was to estimate the number of background counts present in the region $SX_{min} \leqslant 0.05\ \mathrm{cm}^2$ in each bin of x_F and p_T.

A study of the SX_{min} distributions in the x_F regions above that of the x_F/p_T box cut was undertaken to ascertain whether the shape of the background distributions varied with x_F. The ratios of counts in the SX_{min} region $0.16 \leqslant SX_{min} \leqslant 0.32\ \mathrm{cm}^2$ to counts in the region $SX_{min} \leqslant 0.05\ \mathrm{cm}^2$ from $\pi^{\pm}$ data in several high-x_F bins (see Table VIII) show no evidence for an x_F dependence in the background or a difference between π^+ and π^-. (The ratio did differ for proton data, however.)

Numerical estimates show a clear growth in background with increasing x_F for all three particle types. The background fractions were largest for π^- (ranging from 4% at small x_F to 70% at large x_F) and smallest for protons (ranging from 1.5% to 4.5% over the region of interest). The estimated systematic error in the background calculation method was 9% for $\pi^{\pm}$ and 32% for protons.

B. Track reconstruction method B

A different analysis method was used that employed a simple algorithm for track reconstruction which was much faster than method A. Two types of events were analyzed.

The first one was as follows. It was demanded that each plane of the x hodoscopes have only one hit (hits in two adjacent cells were regarded as a single hit). This gave only two possible tracks, one before the analysis magnet and one after. If these hodoscope hits came from a good event they would have intersected near the z coordinate of the center of the magnet. A typical distribution of the track separation in x (x_{diff}) at the center of the analysis magnet is shown in Fig. 10. Fitting a Gaussian form to this curve gives a mean value of zero and a σ of 4 mm. This and similar distributions were used to estimate backgrounds.

The second type of event used had only one hit in any of three x planes and two non-adjacent hits in the fourth plane. This type of event was found about 30–40 % as often as the first type of event. To reconstruct this event the following procedure was performed. Under this criteria there was an unambiguous track either before or after the analysis magnet. On the other side of the magnet there were two possible tracks. We chose the one that gave the smallest x_{diff} at the center of the magnet.

Cuts on the following parameters were applied to select good tracks for the asymmetry calculation: (1) x difference of the crossing of two straight tracks at the center of the magnet, and (2) z coordinate of the track at the target (B_z).

Background estimate

To estimate the background, the tails of the x_{diff} distribution (out of the region $-12\ \mathrm{mm} < x_{diff} < 12\ \mathrm{mm}$) were fitted by a constant. This fitting parameter was used to subtract the background under the peak. There was no hint that the background increased in our region of interest (unlike method A). Crude estimates gave the following: for π^+ the background is less than 1.5% in all x_F bins; for π^- the background is less than 1.5% at $x_F < 0.7$, equal to 2.1% at $0.7 < x_F < 0.75$, and rises up to 4.6% at $0.75 < x_F < 0.8$. Because these values are all so small, it was decided not to do a background subtraction for method B.

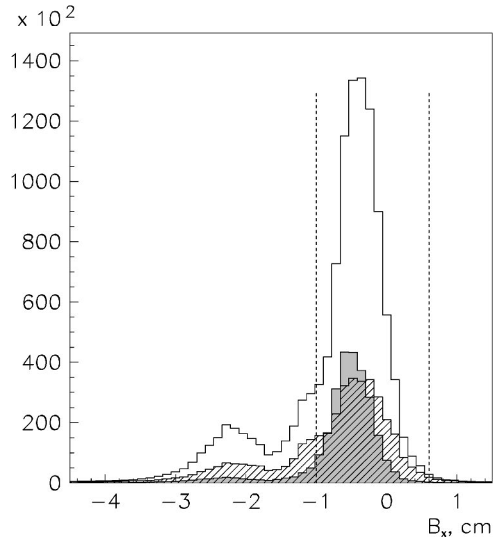

FIG. 7. Distributions of the parameter B_x from the tracking algorithm (x intercept of track at $z=0$) in method A. The top trace is from π^+ data, the hatched region is from π^- data, and the gray region is from proton data. The indicated cuts selected events from the carbon target, which produced the large peak. The peak at $B_x = -2.2$ is from tracks originating in the CH_2 target of the elastic polarimeter farther upstream.

C. ADC and TDC cuts on the data

To save computing time, an initial crude cut on the Čerenkov ADC spectra of the data for B magnet polarity was applied (see Table V). Figure 11 shows a Čerenkov ADC spectrum for a "π^+" run, where the Čerenkov counter was in the trigger. The cut at channel 70 eliminated events in the pedestal region (sharp spike at left) where zero pulse height was recorded by the ADC. For "proton" mode with the Čerenkov counter out of the trigger, the ADC spectrum was dominated by events in the pedestal coming from protons. Line 1 of Table VI shows the number of events which survived the initial Čerenkov ADC cuts.

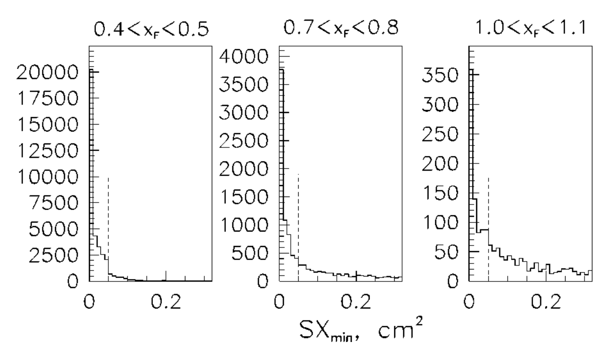

FIG. 8. Distributions of SX_{min} in three different x_F bins for π^- data from method A. The hard cut below 0.05 is indicated by dashed lines.

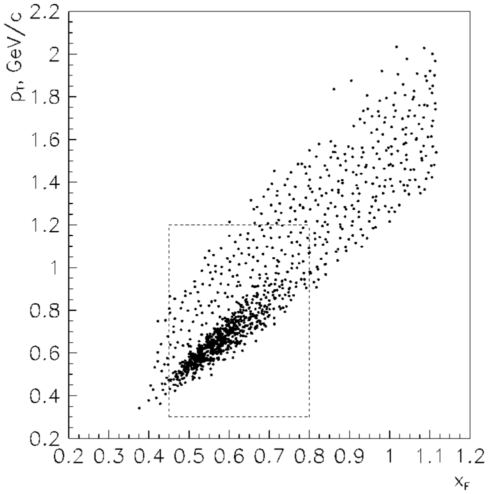

FIG. 9. Scatter plot of x_F vs p_T. The box indicates the cuts on x_F and p_T. This was the final cut before background subtraction in method A.

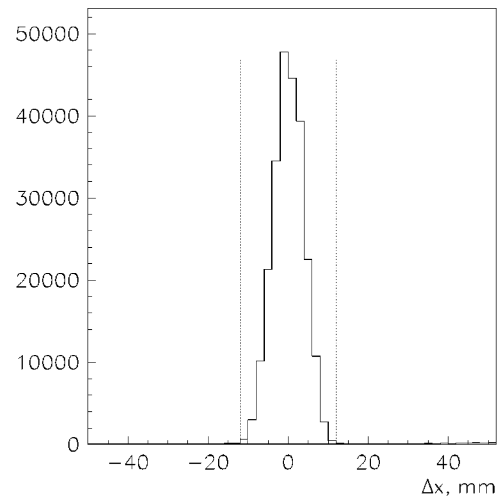

FIG. 10. Distribution of the difference in the x coordinates of the two tracks at the magnet center in method B. Vertical lines indicate cuts applied in the analysis.

Figure 12 shows the S1/S3 time of flight (TDC2) for the remaining events. The tails of this distribution were cut out at channels 620 and 840 (time per channel $=0.05$ ns). The S1/Čerenkov time of flight (TDC1) is shown in Fig. 13. Protons were not seen by the Čerenkov counter, so the proton requirement at this stage was that the TDC for the Čerenkov counter had overflowed, having not received a stop signal. For π^+, a cut between channels 640 and 840 was applied; no cut was applied for π^- in method B. Although the flight path from S1 to S3 was 9.10 m, the differences in time of flight for various particle types were still too small to distinguish particles in the experiment because the tracks had momenta of the order of 10 GeV/c. The primary function of the S1/Čerenkov cut was to eliminate background in the π^+ signal. Numbers of counts which passed the time of flight cuts are in lines 5 and 6 of Table VI.

Cuts were next applied to the Čerenkov ADC spectra of particular x_F bins of the π^+ data to remove K^+ contamination. Figure 14 shows the result of subtracting a π^- ADC spectrum from a π^+ ADC spectrum after normalizing the π^- data to that of the π^+ in the region above channel 400. The excess below channel 300 in the figure is due to K^+ contamination in the "π^+" signal. The size of the K^+ background varied with x_F, so the Čerenkov ADC cuts for kaon suppression also varied. Below x_F of 0.55 no cuts were applied, for $0.55\leqslant x_F\leqslant 0.6$ events below channel 200 were rejected, and for $x_F>0.6$ the cut was placed at channel 300 (see Fig. 11). No cuts for kaon rejection were applied in the π^- or proton data sets. The estimated remaining K^+ contamination in the "π^+" sample after the ADC cuts was less than 2%. While in proton mode, the Čerenkov counter vetoed the trigger which automatically eliminated most of the pions and kaons.

TABLE VIII. Ratios of the numbers of events in the region $SX_{min}<0.05$ cm^2 to the numbers of the events in the tail region $0.16<SX_{min}<0.32$ cm^2 using method A (carbon target).

Reaction	Kinematically forbidden region	Ratio
π^-	$0.85<x_F<0.92$	2.41 ± 0.13
π^-	$0.92<x_F<1.00$	2.49 ± 0.16
π^-	$1.00<x_F<1.10$	2.56 ± 0.18
π^+	$0.92<x_F<1.00$	2.47 ± 0.21
π^+	$1.00<x_F<1.10$	2.30 ± 0.23
Average ratio		2.45 ± 0.08

D. Calculation of analyzing powers

The formula used to calculate inclusive analyzing powers A_N was

$$A_N=\frac{1}{P_b}\left[\frac{n_- - n_+}{n_- + n_+}\right]\left[\frac{n_- + n_+}{n_- + n_+ - 2n_{back}}\right], \qquad (5.13)$$

where $n_\pm$ was given by the ratio of the raw counts in a given x_F/p_T bin to counts in the LOR luminosity scaler:

$$n_\pm=\frac{N_\pm}{\mathrm{LOR}_\pm}. \qquad (5.14)$$

The method assumed that the background rates were the same for both beam states. The apparent sign change in Eq. (5.13) compared to Eq. (1.1) occurred because the inclusive particle was detected to beam-right instead of beam-left.

Counts for LOR were taken from a scaler module which was gated off whenever the data-acquisition computer was busy reading out event information from the hodoscopes. Note that the correction factor in Eq. (5.13) could affect the magnitude of A_N, but not its sign.

E. Comparison of the results of the two methods

We did a comparison of the two methods by using each method to analyze the carbon data from 1997. A comparison

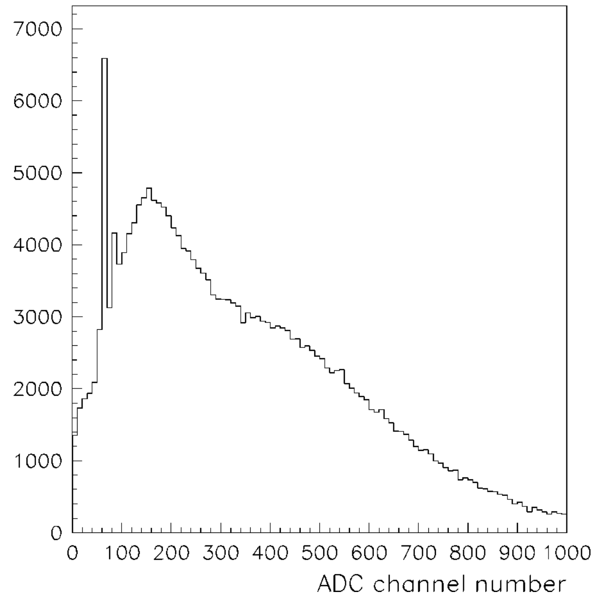

FIG. 11. Raw ADC spectrum from the Čerenkov counter for the π^+ running mode, where the Čerenkov counter was in the trigger. For π^+, events above the pedestal were selected by an initial cut at channel 70. For protons, only events below channel 70 were used.

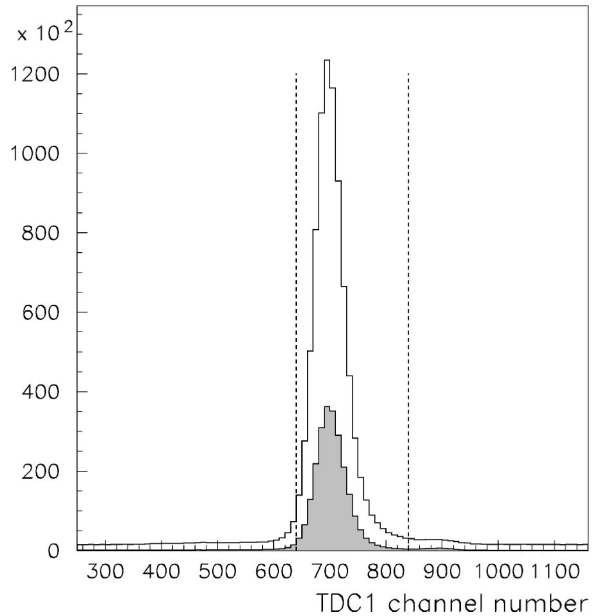

FIG. 13. Time of flight from S1 to the Čerenkov counter. The upper and lower traces are for π^+ and π^- running modes, respectively. Vertical lines indicate cuts applied in the analysis.

of the results is shown in Table IX. There is good agreement between the methods, but method B reconstructs more events (about 30% for π^-, since no cuts on the Čerenkov counter ADC or TDC were made, and the backgrounds are less). So the errors for π^- are noticeably less at large x_F.

A peculiarity of method B is that it only reconstructs events with small multiplicity (1 or 2). The portion of such events was about 48% for π^+ and 25% for π^-. It should be understood that by excluding the events with higher multiplicity we are in the realm of the ''semi-inclusive'' processes. However, our comparison of the results from method A shows that the high multiplicity events are mostly background ($\approx 7\%$ good events for both $\pi^+$and π^-).

Since the two methods gave close results for both π^+ and π^-, method B was chosen as the primary method for analyzing the data due to its speed, simplicity, and low background. Method A provided a useful check showing that the multiplicity restrictions of method B do not change the results.

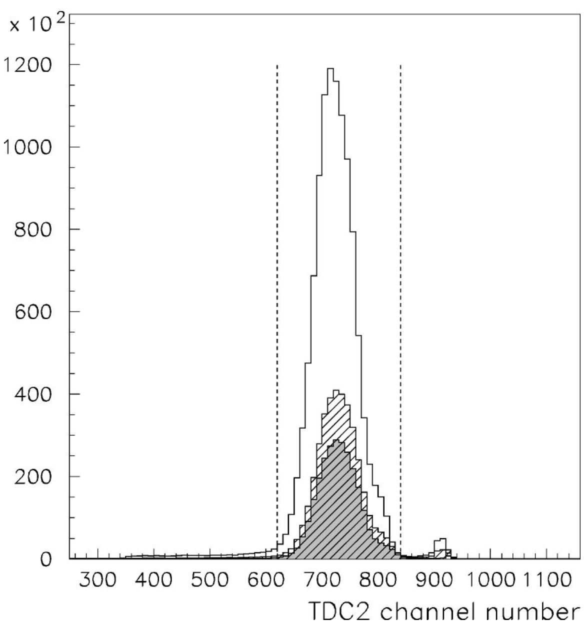

FIG. 12. Time of flight from S1 to S3. The top trace is from π^+ data, the hatched region is from π^- data, and the gray region is from proton data. Vertical lines indicate cuts applied in the analysis.

F. Analysis of the hydrogen data

There were no changes to the apparatus or electronics for this run. The momentum was slightly different at 21.92 GeV/c and the p_T kick of the magnet was different, being 0.86 GeV/c instead of 0.95 GeV/c. The integrated luminosity monitor numbers LOR_+ and LOR_- used in the asymmetry calculations are given in Table X.

There were two types of triggers used. First we used a trigger requiring that three out of four x planes (3/4) of the hodoscopes had hits and second, we had a trigger requiring that all four x planes had hits (4/4). The number of triggers of each type are shown in Table XI.

The portion of the events which could be analyzed by method B (either only one hit in each plane or two hits in one plane and only one hit in each of the other three planes) were as follows: 3/4 trigger: 46% for π^+ and 20% for π^-; 4/4 trigger: 82% for π^+ and 75% for π^-. These values are similar to the corresponding ones for the carbon data treated by method A, where only the 3/4 trigger was used.

We were also able to detect inclusive events from the CH_2 target used to monitor the polarization. Figure 15 shows the distribution of the z coordinate of our reconstructed track when projected back to the target $(x=0)$. (Note, Fig. 7 gives

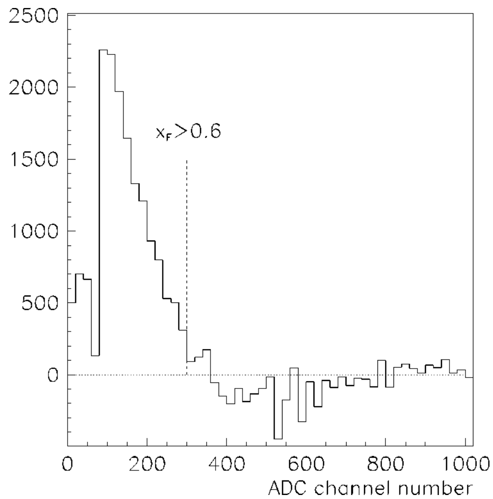

FIG. 14. Difference of Čerenkov ADC spectra of π^+ and π^- data in the region $x_F > 0.6$ normalized in the range above ADC channel 400. The excess at the low end is due to K^+ contamination in the π^+ sample. The vertical line indicates the cut applied to the π^+ data to reject kaons.

the projected x position at $z=0$ rather than the projected z position at $x=0$.) The peak near zero is from the hydrogen target and the other peak comes from the CH_2 target. We had similar numbers of events from each target, but due to acceptance differences the hydrogen target had more high x_F and fewer small x_F events than the CH_2 target.

For this run only method B was used to analyze the data. The following cuts were applied to select pions for the asymmetry calculation:

(1) $620 < \mathrm{TDC2} < 840$ for the S1/S3 time of flight (identical to the carbon target cuts),

(2) -12 mm$< x_{diff} <12$ mm for the track matching at the magnet center (also the same as for carbon target runs),

(3) z coordinate at the target should be -10 cm$< B_z < 20$ cm for the hydrogen target and -30 cm$< B_z < -10$ cm for the CH_2 target.

For π^+ the additional cuts were (4) $720 < \mathrm{TDC1} < 880$ for the S1/Čerenkov time of flight, and (5) Čerenkov ADC >200 for $0.55 < x_F < 0.6$ and ADC>300 for $x_F > 0.6$. This latter cut was identical to that used for carbon target data, and was employed to reject K^+ contamination. The result of applying these cuts is shown in Table XI.

G. Analyzing power results

The results for the analyzing powers A_N for π^- and π^+ produced on hydrogen and for protons produced on carbon binned in both x_F and p_T are presented in Tables XII, XIII, and XIV, respectively. The uncertainties include statistical errors and do not include a 25% relative error for the carbon run and 14.5% for the hydrogen run coming from the uncertainty in the absolute beam polarization obtained from the *pp* elastic polarimeter. Studies of systematic errors in the inclusive setup indicated that they were small compared to the statistical errors of the asymmetries alone. Details of cross-checks are presented in Sec. V H.

TABLE IX. Analyzing power A_N (in percent) for π^+ and π^- on the carbon target at 21.6 GeV/c.

$\langle x_F \rangle$	π^+ Method A	π^+ Method B	π^- Method A	π^- Method B
0.48	3.2 ± 1.6	2.1 ± 1.7	3.2 ± 2.2	4.8 ± 2.0
0.53	5.8 ± 0.9	6.1 ± 0.9	2.1 ± 1.4	2.1 ± 1.3
0.57	12.2 ± 1.1	12.5 ± 1.1	-1.6 ± 1.6	-0.4 ± 1.4
0.62	21.0 ± 1.6	22.8 ± 1.5	-9.0 ± 2.3	-11.3 ± 2.0
0.67	30.4 ± 2.4	30.2 ± 2.4	-24.2 ± 4.2	-26.1 ± 3.4
0.72	43.6 ± 4.3	44.0 ± 4.0	-28.8 ± 9.2	-43.6 ± 6.5
0.77	30.2 ± 8.6	31.0 ± 8.1	-47.3 ± 27.9	-30.5 ± 13.4

Because x_F and p_T are correlated variables, it was of interest to see if A_N depended more on the one variable or the other within the limits of the inclusive spectrometer acceptance. For the π^- and π^+ data, Figs. 16 and 17 show A_N vs p_T while holding x_F fixed and vice versa. With the exception of the largest p_T bin at 0.88, it is difficult to see much dependence in A_N while holding one variable fixed and varying the other. Similarly, no strong dependence in A_N was observed for the carbon target results. However, integrating over p_T, the values in Table XV and the plot in Fig. 18 are obtained. Clear trends are thereby revealed showing large analyzing powers, opposite in sign for π^- and π^+, and increasing in magnitude at large x_F. The data for protons were consistent with zero in all cases.

The analyzing powers from hydrogen, carbon, and CH_2 as a function of x_F are plotted in Fig. 19. The data appear to be independent of the target, just as for inclusive hyperon polarization results. These are the first measurements for A_N for inclusive pion production versus target material, and suggest that the pion asymmetries are independent of target.

One reason that the carbon target was used in this experiment was to investigate whether a significant asymmetry would be produced. A carbon internal target would also be convenient for polarimetry at RHIC or HERA. However, prior to the results of this experiment, it was possible that pions produced from a nuclear target at a given p_T could be the result of two scatters at smaller p_T within the nucleus [34,35]. Production of pions by multiple scatters could significantly reduce the pion asymmetries from a nuclear target compared to a hydrogen target because the pion asymmetries from hydrogen for smaller p_T are small or zero. The fact that the asymmetries are the same for the two targets, carbon and hydrogen, may provide new information on the dynamics of particle production from a nucleus at moderate p_T.

Comparisons of the data from this experiment with those from other experiments are hampered somewhat by differences in the x_F/p_T acceptances and differences in the target materials used. Only three references in the literature [2,4,36] were found which can be compared with this experiment's carbon results. Other polarized beam or target inclusive measurements in different kinematic regions include Refs. [37,38], as well as other E704 data.

Bonner *et al.* [36] measured A_N on a Be target at 13.3 and 18.5 GeV/c for inclusive π^- and π^+ production in the

TABLE X. Monitor numbers for the 1999 hydrogen run.

Particle and trigger	LOR_+, 10^8	LOR_-, 10^8	LOR_+/LOR_-
π^+ (4/4)	1.6778	1.6767	1.001
π^+ (3/4)	0.1179	0.1179	1.000
π^- (4/4)	3.0080	2.9933	1.005
π^- (3/4)	1.8887	1.8812	1.004

small x_F region below 0.6. They observed no differences between incident momenta of 13.3 and 18.5 GeV/c. The new data at 22 GeV/c from the present experiment are in good agreement, showing A_N values consistent with zero for π^- and rising to around 10% at $x_F=0.6$ for π^+.

Dragoset *et al.* [4] measured A_N on hydrogen and deuterium targets for inclusive π^- and π^+ at 11.75 GeV/c. There is, however, only a small overlap in x_F and p_T between the Dragoset π^+ data and those from the present experiment at 22 GeV/c. (The data for π^- do not overlap.) The Dragoset π^+ data at 11.75 GeV, replotted in x_F and p_T, are compared to the present 22-GeV/c data in Figs. 20 and 21. Both data sets show a similar x_F dependence, with the data at 11.75 GeV/c being smaller in magnitude.

Finally, Adams *et al.* [2] measured A_N on a hydrogen target for inclusive π^- and π^+ production at 200 GeV/c. The comparison of the 200-GeV/c data with the present 22-GeV/c data in Fig. 22 shows that the general shape of A_N as a function of x_F looks similar over the RHIC beam energy range, with π^+ being positive and π^- being negative. The 200-GeV/c data were integrated over an acceptance of $0.2 \leq p_T \leq 2.0$ GeV/c, which is larger than the $0.3 \leq p_T \leq 1.2$ GeV/c range of the present experiment at 22 GeV/c.

H. Systematics studies of inclusive data

1. Luminosity monitor systematics

In Sec. IV A it was pointed out that luminosity monitors should be stable and as free as possible from the influence of

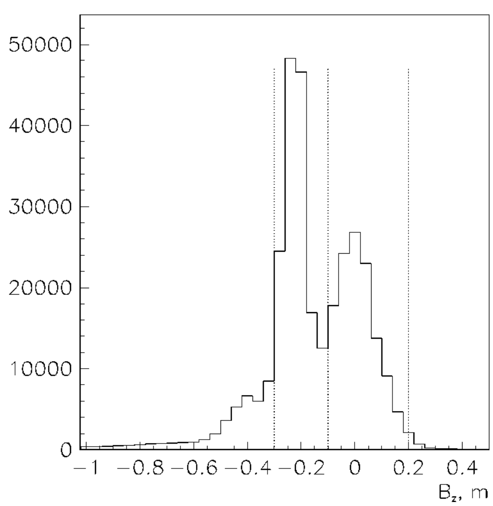

FIG. 15. Distribution of the track z coordinate at the targets from method B. Dotted lines indicate the cuts applied. The small peak is produced by the hydrogen target. The large peak is produced by the elastic target. Note this is a different variable than shown in Fig. 7.

TABLE XI. Number of events for π^+ and π^- before and after the cuts were applied for the hydrogen target using method B.

Particle and trigger	Full number of events	Number of events after cuts
π^+ (4/4)	1 020 478	163 492
π^+ (3/4)	191 736	11 543
π^- (4/4)	543 361	123 936
π^- (3/4)	1 262 825	70 256

the beam polarization. The luminosity telescopes were in the vertical plane at the lab angle corresponding to 90° in 1997 for *pp* elastic scattering—a position deliberately chosen to minimize sensitivity to beam spin effects. The up/down asymmetries of counts in the luminosity arms, for scattering off the carbon target, calculated using the square root formula of Eq. (3.2) were $(7.5\pm5.2)\times10^{-5}$, $(5.2\pm5.9)\times10^{-5}$, and $(1.4\pm3.7)\times10^{-4}$ for the π^-, π^+, and proton data, respectively. (The numbers for scattering off hydrogen were consistent with zero.) There was thus no evidence for any spin dependence in the luminosity monitors at a level about four orders of magnitude below the level of the asymmetries observed in the inclusive spectrometer. The stability of the luminosity monitors (and of the vertical direction of the beam spin axis) is illustrated in Fig. 23, which shows the up/down asymmetry as a function of increasing run number (i.e. time) during the run with the carbon target. There were no significant deviations from zero.

2. Time stability of inclusive asymmetries

The value of the beam polarization obtained from the elastic polarimeter was produced by integrating the counts over all of the running periods to maximize the elastic statistics. To check for time fluctuations in the beam polarization, the inclusive data for π^- and π^+ were divided into roughly equal time intervals of several hours each. Figure 24 shows the analyzing power results for two different x_F bins as a function of time. (Note: These data points include the factor of $1/P_b$ in the values, but the uncertainties do not include the contribution from the uncertainty in the beam polarization.) No significant fluctuations were observed, and the observed fluctuations are not correlated between the two x_F bins shown. There was thus no evidence for time-dependent fluctuations in the beam polarization on the scale of a few hours to days.

3. Relative differential cross sections

As a check to make sure the x_F distributions of the observed scattering had the right shape and that they were not being skewed by kaon contamination or other factors, unpolarized differential cross sections were calculated from the inclusive data. Because the experiment was not designed to measure absolute cross sections, relative cross sections were calculated. The overall normalization was adjusted to match the π^- data point at $x_F=0.53$ to the corresponding point in the 24-GeV/c Be target data of Eichten *et al.* [39]. The same normalization constant was then used for all other data points for π^-, π^+, and protons.

TABLE XII. Asymmetry A_N (in percent) in π^- inclusive production on the hydrogen target at 21.92 GeV/c. The systematic uncertainty of $\pm 14.5\%$, coming from the uncertainty on P_b, is not included.

p_T \ x_F	0.48	0.53	0.57	0.62	0.67	0.72
0.53	-4.7 ± 4.8					
0.58	3.9 ± 2.7	-5.7 ± 7.4				
0.63	-1.9 ± 3.6	-2.8 ± 2.5				
0.68		0.6 ± 2.0	8.9 ± 3.4			
0.73		1.9 ± 3.5	-0.9 ± 2.5	-12.3 ± 8.3		
0.78			0.4 ± 2.6	-8.5 ± 4.1		
0.83			-11.7 ± 4.3	-12.4 ± 3.9	-19.0 ± 7.0	
0.88				-13.1 ± 4.1	-21.7 ± 7.0	-34.0 ± 19.6
0.93				-23.2 ± 6.4	-31.6 ± 6.3	-18.8 ± 12.9
0.98					-29.8 ± 7.6	-23.5 ± 11.2

The relative cross sections were calculated using a formula which is proportional to the invariant cross section for particle production:

$$E\frac{d^3\sigma}{dp^3}\propto\sigma_{rel}(x_F)=C_{norm}\left\{\frac{1}{p_{max}I_{beam}}\right\}\times\left[\frac{\langle E\rangle N_{events}}{\langle p_T\rangle\varepsilon\Delta p_T\Delta x_F}\right]. \tag{5.15}$$

In Eq. (5.15), all the x_F-dependent terms have been grouped in the square brackets. All such terms were averaged over p_T and/or x_F within a given x_F bin. The terms which are independent of x_F, but dependent on an inclusive particle type, are grouped in the curly brackets, and all factors which depend neither on x_F nor on inclusive particle type are combined into the relative normalization constant C_{norm}. The x_F-dependent terms are $\langle E\rangle$, the average total energy of the inclusive particle in the c.m. frame within the x_F bin, N_{events}, the sum (after background subtraction) of inclusive counts of both beam spin states, $\langle p_T\rangle$, the average p_T within the x_F bin, ε, the geometric acceptance as a fraction of 4π obtained from the Monte Carlo simulation, Δp_T, the width of the p_T distribution within the x_F bin, and Δx_F, the width of the x_F bin. The terms in the curly brackets are p_{max} from the definition of x_F in Sec. V, and I_{beam}, the number of counts in the upstream ion chamber scaler multiplied by the computer live time and summed over both beam spin states for beam normalization. The beam telescopes could not be used because they were not calibrated to give the absolute number of beam particles. The upstream ion chamber was not sensitive to the spectrometer magnet polarity. Because of the narrowness of the acceptance of the inclusive spectrometer, the efficiency was assumed to have been independent of x_F and an inclusive particle type, and it is therefore part of C_{norm}, together with the target thickness and density and other constant factors.

No correction was applied for events which might have originated from sources other than the primary target. During the running, "empty-target" runs with the carbon block removed were performed to estimate the rate for non-carbon events. The ratio of event rates for "empty-target" vs carbon runs was found to be about 0.02, so the non-carbon background was considered to have been negligible for the purposes of the relative cross-section calculation. The empty to full target ratio for hydrogen was ~ 0.10. Based on the inclusive cross sections for K^- and $\bar{p}$ production, the non-

TABLE XIII. Asymmetry A_N (in percent) in π^+ inclusive production on the hydrogen target at 21.92 GeV/c. The uncertainty given does not include the systematic uncertainty of $\pm 14.5\%$ coming from the uncertainty of P_b.

p_T \ x_F	0.48	0.53	0.57	0.62	0.67	0.72
0.53	7.7 ± 5.4					
0.58	4.3 ± 3.0	-6.5 ± 8.0				
0.63	1.3 ± 3.7	2.9 ± 2.5				
0.68		8.4 ± 2.0	16.7 ± 3.5			
0.73		12.8 ± 3.2	11.8 ± 2.4	13.6 ± 8.4		
0.78			15.5 ± 2.5	20.8 ± 3.9		
0.83			26.9 ± 4.3	26.3 ± 3.7	29.2 ± 6.1	
0.88			17.1 ± 11.7	27.6 ± 3.8	32.8 ± 5.8	60.5 ± 16.4
0.93				19.4 ± 5.9	24.0 ± 5.2	38.4 ± 9.1
0.98					32.1 ± 6.1	39.5 ± 7.6

TABLE XIV. Analyzing power A_N (in percent) for proton inclusive production at 21.6 GeV/c. Errors are statistical only, and do not include the $\pm 25\%$ relative error coming from the uncertainty in P_b. This is for a carbon target using method A.

p_T \ x_F	0.48	0.53	0.57	0.62	0.67	0.72
0.48	2.9 ± 8.1					
0.53	-1.2 ± 4.6	-7.0 ± 5.0				
0.58	-12.0 ± 11.8	2.1 ± 2.6	3.8 ± 6.0			
0.63		0.1 ± 4.0	2.8 ± 3.0	-5.0 ± 10.0		
0.68		1.9 ± 11.9	-0.2 ± 2.8	-2.2 ± 3.4		
0.73			6.3 ± 4.9	-1.3 ± 3.2	-4.8 ± 4.6	
0.78				-6.1 ± 3.8	3.3 ± 4.1	6.5 ± 9.6
0.83				1.6 ± 6.0	-0.8 ± 4.2	6.1 ± 6.1
0.88					-7.1 ± 5.4	4.6 ± 5.4
0.93					9.2 ± 9.3	-0.4 ± 6.2

pionic contributions to the π^- event sample were estimated to have been less than 3%. Consequently, corrections for non-pionic contributions were also not included in the calculation. Figure 25 shows the good agreement of the derived x_F dependences of the relative cross sections with those of the Eichten data.

VI. THEORETICAL DISCUSSION

From recent experiments it is known that mesons produced by colliding polarized protons on nuclear targets at medium and high energies exhibit large analyzing powers at large x_F and small p_T, as do the present results at 22 GeV/c. Large polarizations have also been observed in hyperon production. (See, e.g. [10] for an extensive list of hyperon and meson production references.) There is a common belief that the large analyzing powers (A_N) in meson production and the polarizations (P_N) in hyperon production are related. The long-range part of the strong interaction may be playing an important role in these experiments. Theories of the mechanism which produces the observed large analyzing powers in meson production are expected to provide important information about spin-dependent quark dynamics, the momentum distributions of constituents, hadronization, and quark confinement. Currently, however, there is no rigorous model which enables one to systematically interpret the properties of these spin effects. Various theoretical ideas have been proposed to explain the analyzing powers observed in pion production: higher twist effects [40–43], correlation of $k_\perp$ and spin in structure [44,45] and fragmentation [46–49] functions, orbital angular momentum of valence quarks inside a polarized hadron [50–53], and a quark re-

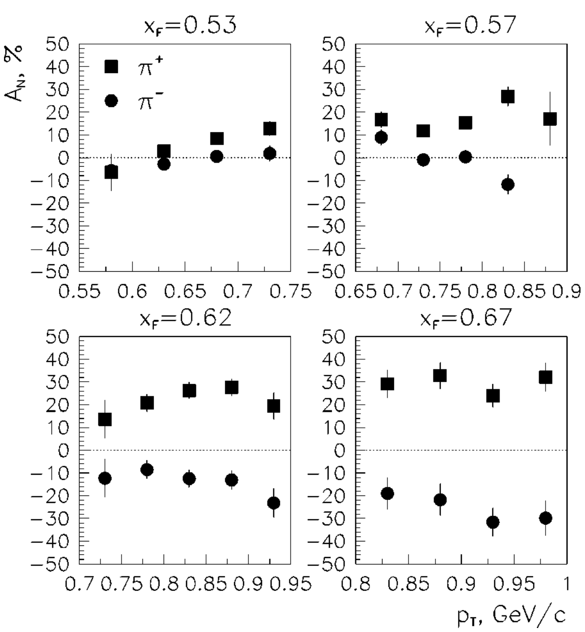

FIG. 16. The p_T dependences of the analyzing power A_N for inclusive π^- and π^+ production at 22 GeV/c within four bins of fixed x_F off of a hydrogen target.

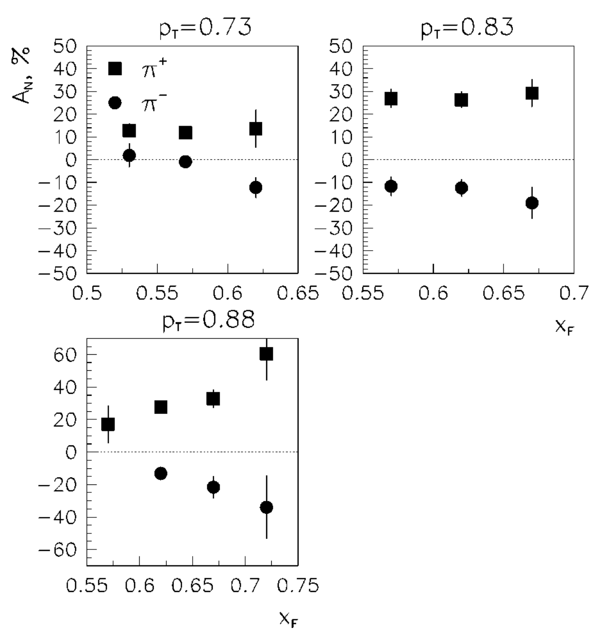

FIG. 17. The x_F dependences of the analyzing power A_N for inclusive π^- and π^+ production at 22 GeV/c within three bins of fixed p_T off of a hydrogen target.

TABLE XV. Analyzing powers A_N for π^-, π^+, and protons. Errors are statistical only, and do not include the relative error coming from the uncertainty in P_b.

x_F	$\langle p_T \rangle$(GeV/c)	Target	π^- A_N (%)	π^+ A_N (%)	Protons A_N (%)
0.45–0.50	~0.5	carbon	4.8±2.0	3.7±2.1	−1.6±3.8
		hydrogen	0.7±2.0	3.3±2.5	
		CH_2	2.9±1.1	0.8±1.3	
0.50–0.55	~0.6	carbon	2.1±1.3	5.9±1.1	0.5±2.0
		hydrogen	−0.5±1.4	7.0±1.6	
		CH_2	2.1±1.3	4.7±1.3	
0.55–0.60	~0.7	carbon	−0.4±1.4	12.5±1.1	2.5±1.8
		hydrogen	0.0±1.5	15.4±1.5	
		CH_2	−0.1±1.7	9.8±1.6	
0.60–0.65	~0.7	carbon	−11.3±2.0	22.8±1.5	−2.6±1.8
		hydrogen	−12.9±2.1	23.6±2.0	
		CH_2	−10.7±2.8	16.9±2.7	
0.65–0.70	~0.8	carbon	−26.1±3.4	30.2±2.4	−1.1±2.1
		hydrogen	−25.0±3.3	30.3±2.7	
		CH_2	−25.1±4.9	27.6±4.1	
0.70–0.75	~0.9	carbon	−43.6±6.5	44.0±4.0	2.4±2.9
		hydrogen	−29.6±6.1	42.1±4.3	
		CH_2	−24.7±9.0	42.8±6.7	
0.75–0.80	~1.0	carbon	−30.5±13.4	31.0±8.2	5.9±3.8
		hydrogen	−51.2±11.2	38.7±6.6	
		CH_2	−29.6±17.3	26.9±10.9	

combination model with a relativistic description for the parton-parton interaction [10]. In addition, there is a suggestion that the contribution of instantons to the fragmentation of quarks could lead to single spin asymmetries [54], and there are phenomenological models based on different assumptions for the quark dynamics [55–58].

No theoretical predictions exist for the present results at 22 GeV/c, although a phenomenological model at 13 GeV/c including intermediate particle (Δ) production reproduces some observed features of the data [59]. This momentum is generally considered too low for the models described above to apply. On the other hand, the similarity of these data to the E704 results suggests that a similar mechanism generates A_N for inclusive pion production at both momenta.

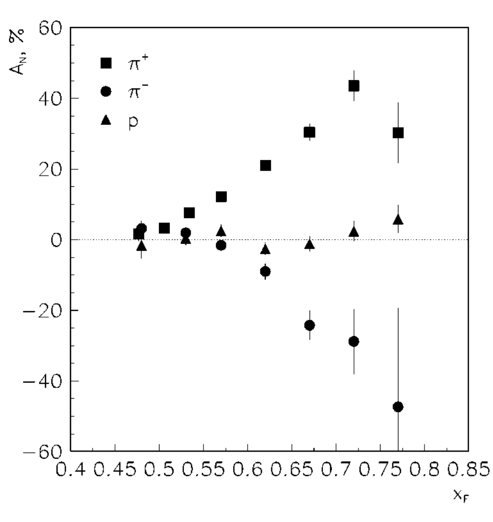

FIG. 18. Analyzing power A_N for π^-, π^+, and proton production on carbon as a function of x_F at 21.6 GeV/c.

VII. CONCLUSIONS

Large analyzing powers were observed for $x_F > 0.5$ and $0.6 < p_T < 1.2$ GeV/c in π^- and π^+ inclusive production on

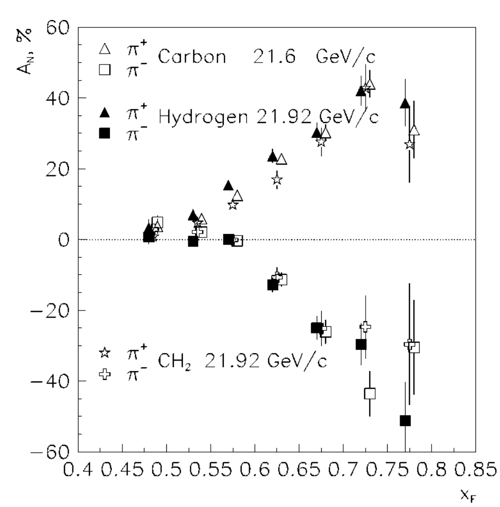

FIG. 19. Analyzing power for π^+ and π^- as a function of x_F on carbon, CH_2, and hydrogen. Note some points are slightly offset from the true value of x_F to make it easier to distinguish the points.

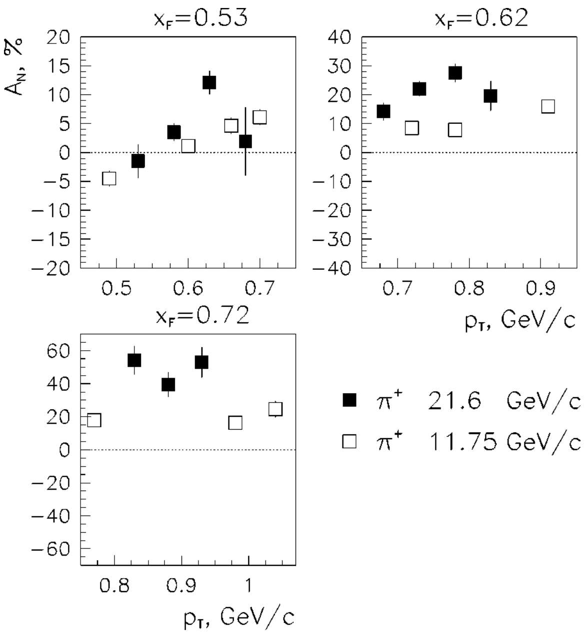

FIG. 20. Comparison of the 21.6-GeV/c π^+ A_N data on the carbon target with 11.75-GeV/c π^+ data [4] at some fixed x_F values.

hydrogen, carbon, and CH_2 with a 22-GeV/c polarized proton beam.

The signs of the inclusive pion production analyzing powers are found to be the same at 22 GeV/c as at 200 GeV/c. The data at both energies exhibit an approximate mirror symmetry as a function of x_F. Data at lower momenta for π^+ mesons are consistent in sign and show a similar rise with x_F. Direct comparisons of π^- inclusive analyzing powers at lower energy were not possible, however, because the kinematic acceptances of the (x_F, p_T) regions covered by the experiments did not overlap.

The 22-GeV/c π^+ inclusive analyzing powers approach zero at higher x_F than at 200 GeV/c, and the 22-GeV/c data

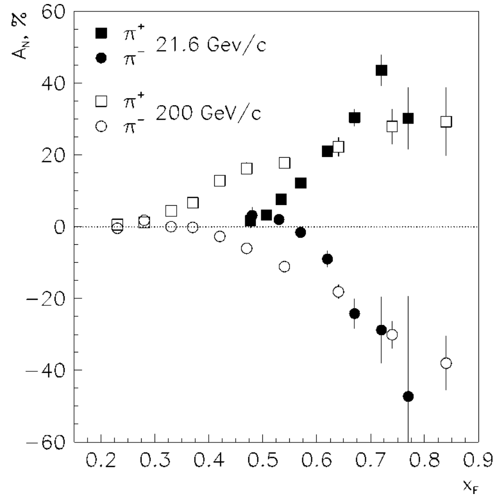

FIG. 22. Comparison of inclusive analyzing powers A_N from carbon at 21.6 GeV/c and hydrogen at 200 GeV/c [2].

rise more steeply. (Note that unlike the slopes of the A_N points, the zero points are independent of the relative error in the beam polarization.) A direct comparison of results at 22 GeV/c and 200 GeV/c is, however, somewhat problematic because of differences in the p_T acceptances of the two experiments. Interestingly, the analyzing powers of π^+ and π^- are the same for both hydrogen and carbon targets (see Fig. 19). This agreement may provide information on the dynamics of particle production from a nucleus at moderate p_T. It appears that one can probably expect to see similar-appearing dependences of A_N vs x_F in the large x_F region throughout the entire RHIC energy range up to 250 GeV/c. Moreover, the analyzing powers are expected to be large.

Inclusive proton production exhibits no measurable asymmetry at 22 GeV/c. Some proton data at lower energy show small analyzing powers (up to 5%) on hydrogen and deuterium targets [21,27,28].

Although the experiment at 22 GeV/c was not set up for

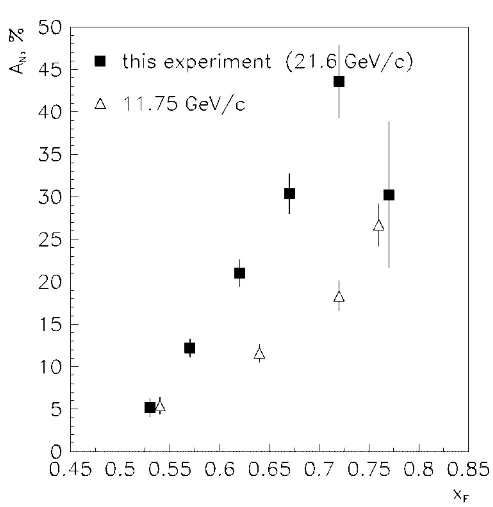

FIG. 21. Comparison of x_F dependences of 21.6-GeV/c A_N data on the carbon target with 11.75 GeV/c [4] in the regions of overlapping p_T.

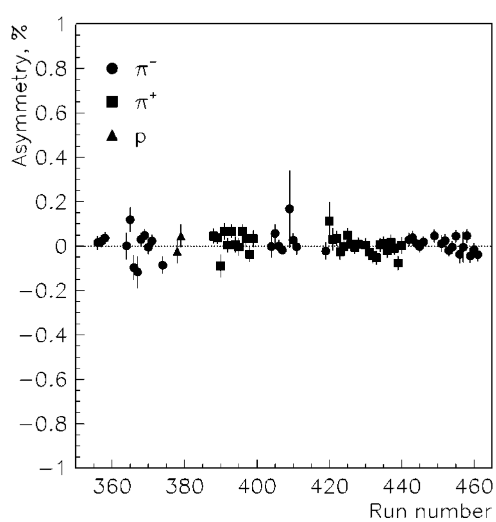

FIG. 23. Up/down asymmetries in the vertical luminosity monitors as a function of an increasing run number during the carbon running.

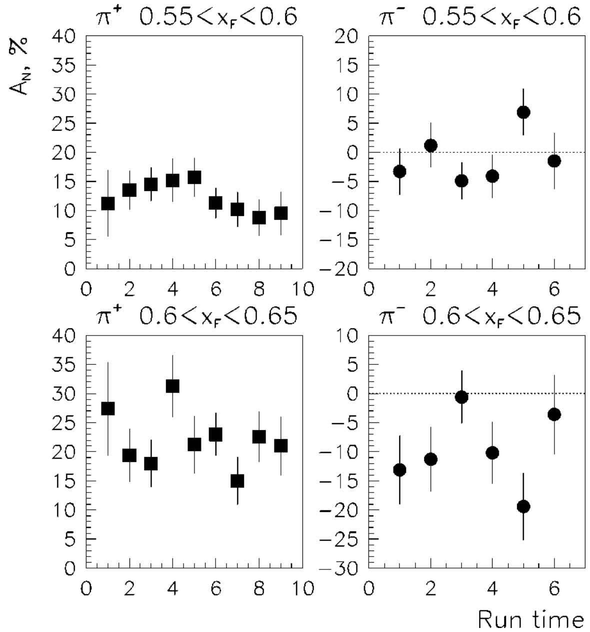

FIG. 24. Analyzing powers A_N in two selected x_F bins as a function of time during the running. The plots at left and at right are for π^+ and π^-, respectively. The upper and lower plots are for $0.55 \leqslant x_F \leqslant 0.60$ and $0.60 \leqslant x_F \leqslant 0.65$, respectively.

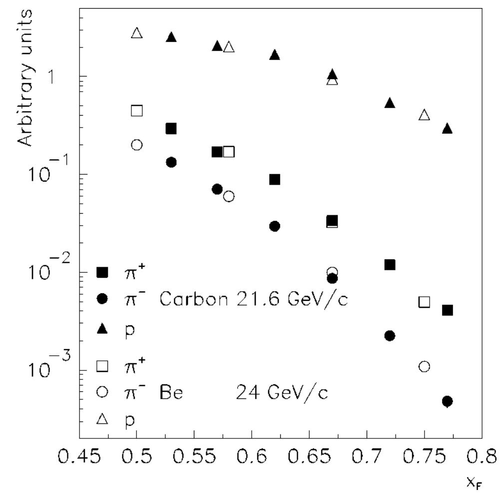

FIG. 25. Relative cross sections of π^-, π^+, and proton inclusive production on carbon as a function of x_F at 21.6 GeV/c compared with the data at 24 GeV/c on a Be target of Eichten *et al.* [39]. The carbon data were normalized to the Eichten results on π^- at $x_F = 0.53$.

measuring absolute cross sections, the relative rates and x_F distributions of unpolarized $\pi^\pm$ and proton production on carbon at 22 GeV/c appear to match analogous data on Be at 24 GeV/c.

The data in this paper complement extensive hyperon-polarization results, and will help efforts to understand the mechanisms that lead to large spin effects at high energy. The new data at 22 GeV/c represent the first strong evidence for large and nearly energy-independent analyzing powers at $x_F > 0.6$ in inclusive charged pion production in the vicinity of the RHIC injection energy. This confirms the attractiveness of these reactions for use in high energy proton beam polarimetry at machines such as RHIC and HERA.

ACKNOWLEDGMENTS

We are grateful to the AGS staff for their assistance with setting up the experiment and operating the accelerator, and to J. Tojo for help with the analysis of the E880 polarimeter data. This project was supported in part by the U.S. Department of Energy, Divisions of High Energy and Nuclear Physics, Contracts W-31-109-ENG-38, DE-FG02-92ER40747, and DE-AC02-98CH10886, and the Russian Ministry of Science and Technology. A portion of this research was performed in the framework of the RIKEN-BNL Collaboration for the RHIC-Spin project. The work of M. Bai was partially supported by Argonne National Laboratory, 9700 S. Cass Avenue, Argonne, IL 60439.

APPENDIX: AGS INTERNAL POLARIMETER

A relative polarimeter was used to monitor the beam polarization in the AGS during this experiment. It was also used previously for tests of the AGS partial snake and RF dipoles [14–18], for polarized beam tuning studies, and for monitoring the polarization for periods when polarized beams were injected into RHIC. This polarimeter was situated in the C20 straight section of the AGS, and it has been operated at beam momenta from ~ 3–24 GeV/c, or slightly above injection to the extraction energy. It was capable of withstanding reasonably high beam intensities, from $\sim 10^{10}$–10^{11} protons per pulse, and was neither very complicated nor expensive. Absolute calibrations have been performed at two low laboratory momenta, as well as at 22 GeV/c from this experiment. The polarimeter design is similar in some ways to a previous internal polarimeter described in Ref. [13]. It is also similar to the recoil arms in the elastic polarimeter for this experiment, and inspired the design for that apparatus.

The AGS internal (E880) polarimeter was designed to detect events with angles and energies consistent with *pp* elastic scattering. The polarized beam struck an internal nylon or carbon target. Left and right symmetric arms centered at $\theta_{lab} \sim 77.25°$ were constructed as illustrated in Fig. 26. The recoil particles in each arm traversed a pair of plastic scintillation counters (L_1, L_2 or R_1, R_2 at 27.3 and 40.0 cm from the nominal target position), a seven-element scintillation counter hodoscope, an aluminum wedge-shaped degrader, and a thick plastic scintillator (L_3 or R_3 located 114.0 cm from the target). The polarimeter was to be operated so that protons from *pp* elastic scattering would stop in L_3 or R_3 over the full laboratory angular acceptance of $\pm 1.3°$. Many charged pions would pass through these counters and strike the veto scintillation counters V_L or V_R. The aluminum wedges could be moved remotely in order to place them at optimal locations as a function of beam momentum to match *pp* elastic scattering kinematics.

The polarimeter targets were located in the accelerator vacuum. They were swung into the beam every AGS cycle, at the beginning of the flat-top or front porch energy, when the beam momentum was essentially constant for at least 0.5 sec. Measurements began soon after the target was in the beam, and they ended before the accelerator energy was changed. The nylon target ($C_6H_{11}NO$) was spooled with two dc motors at ~ 30 cm/sec to minimize heat and radiation damage; the nylon would break when sufficient damage occurred. Nylon in the form of monofilament string (~ 0.1 mm diameter fishline) was used. The targets were inhibited from swinging into the beam when the spooling direction was being reversed, or when a sensor indicated that the beam intensity was too high. A carbon target was formed of four (one) individual 30-μm diameter fibers during the inclusive measurements from the carbon (liquid hydrogen) target. (Three strands were used in runs during July 1997. A smaller diameter fiber, 8 μm, was used at other times; 35 strands in April and December 1994, 10 strands in July 1996, and 2 strands in September 2000.) The carbon fiber(s) were glued onto the same target holder ~ 2.5 cm away from the nylon target. The target position could be adjusted remotely; rates in the polarimeter arms were recorded as the target was scanned across the beam in different beam pulses. This allowed the locations to be determined to center either the nylon or carbon target on the beam. Such scans were required after changes in the accelerator energy or after major changes in the AGS operating conditions.

Various singles and coincidence rates were scaled from the left and right arms, and some asymmetries computed using the square root formula in Eq. (3.2). One of the scaled quantities was similar to that from the previous AGS polarimeter [13]. For the left arm, it was designated $L_{OLD} = L_1 \cdot L_2 \cdot L_3$. A similar quantity, R_{OLD}, was formed for the right arm, and the calculated asymmetry was denoted ϵ_{OLD}. Two other types of quantities, denoted L_{F1}, R_{F1} and L_{F2}, R_{F2} were also generated electronically and scaled. These had requirements on the correlation of the encoded hodoscope number and the pulse height in L_3 or R_3 (also encoded by a commercial flash analog-to-digital converter). These correlations were computed if a trigger condition was satisfied, involving the coincidence $L_1 \cdot L_2 \cdot L_3 \cdot H_L \cdot \overline{V_L}$ and similarly for the right polarimeter arm. The signal H_L designates one, and only one, hodoscope counter having triggered its discriminator. The asymmetry with the least background from nonelastic processes was ϵ_{F1}, and the one with the largest background was ϵ_{OLD}.

The DAQ system for the AGS internal polarimeter was very similar to those used to record the inclusive and elastic events in this experiment, and actually predated them. The scaled quantities, included singles and coincidence rates and accidentals, were read at the end of each AGS cycle, summed with counts from previous spills, stored, and asymmetries calculated. Typically one event per spill was read in to monitor the hardware performance, which introduced a small deadtime. Histograms of the correlations for L_{Fi} and R_{Fi} and of other quantities were also made. Typical runs lasted ~ 15 min and resulted in statistical uncertainties of $\delta\epsilon_{OLD} \sim \pm 0.0003$ and $\delta\epsilon_{F1} \sim \pm 0.0005$.

The polarimeter was calibrated at beam momenta of 5.4 and 7.5 GeV/c by using measured target thicknesses and asymmetries observed with the nylon and carbon targets (Ref. [14]). The asymmetries with low background, ϵ_{F1} and ϵ_{F2}, were important to measure the true pp elastic-scattering asymmetry, but they relied on a careful tuning of the correlation cuts. The beam polarization was then found using the analyzing powers from the fit in Ref. [22]. Then the effective analyzing powers for ϵ_{OLD} with the nylon target could be determined, and were found to be

$$A_{OLD} \simeq 0.0439 \pm 0.0013, \quad P_{lab} = 5.4 \text{ GeV}/c \tag{A1}$$

$$\simeq 0.0374 \pm 0.0052, \quad P_{lab} = 7.5 \text{ GeV}/c. \tag{A2}$$

Assuming no difference in the average beam polarization between the beam sampled by the AGS internal polarimeter and that sampled in the elastic-scattering measurement in this experiment, then

$$A_{OLD} \simeq 0.0172 \pm 0.0027, \quad P_{lab} = 21.9 \text{ GeV}/c. \tag{A3}$$

With higher beam intensities from a new optically

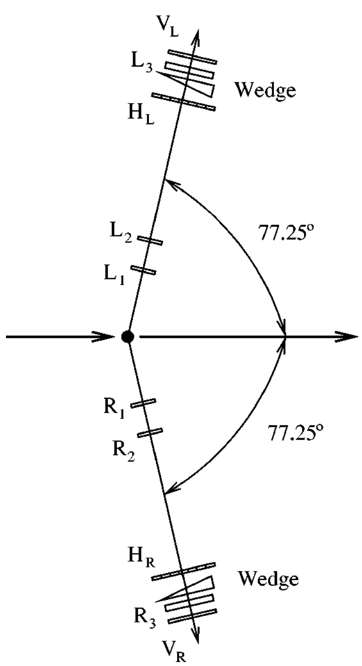

FIG. 26. Schematic layout of the AGS internal polarimeter.

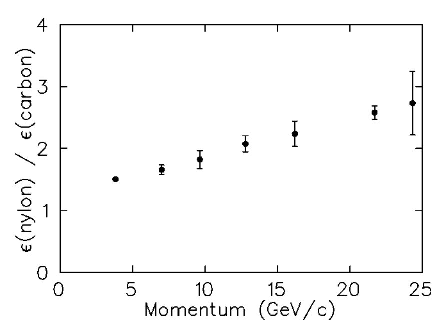

FIG. 27. Ratio of asymmetries for the nylon and carbon targets observed with the AGS internal polarimeter. Recent data suggest that the ratios at the lowest one or two momenta may be artificially small.

pumped polarized ion source for the AGS and RHIC, the existing nylon target will be damaged very rapidly. The carbon fibers will withstand these conditions, and thus will be used in the future with the AGS internal polarimeter. Measurements of the ratio of asymmetries for nylon and carbon targets were made during these experiments and in the past, and are plotted in Fig. 27. The ratios at the lowest one or two momenta may be artificially low due to large beam sizes in the AGS at these energies, and the proximity of the carbon and fishline targets. This information was employed in the estimation of carbon contamination to the elastic scattering measurements; see Sec. III B 5.

[1] G.L. Kane, J. Pumplin, and W. Repko, Phys. Rev. Lett. **41**, 1689 (1978).
[2] D.L. Adams *et al.*, Phys. Lett. B **264**, 462 (1991).
[3] A. Bravar *et al.*, Phys. Rev. Lett. **77**, 2626 (1996).
[4] W.H. Dragoset *et al.*, Phys. Rev. D **18**, 3939 (1978).
[5] D.L. Adams *et al.*, Phys. Lett. B **261**, 201 (1991).
[6] D.L. Adams *et al.*, Z. Phys. C **56**, 181 (1992).
[7] D.L. Adams *et al.*, Nucl. Phys. **B510**, 3 (1998).
[8] K. Heller, in *Proceedings of the 12th International Symposium on High-Energy Spin Physics, Amsterdam, 1996*, edited by. C. W. de Jager *et al.* (World Scientific, Singapore, 1997), p. 23.
[9] L. Zuo-tang and C. Boros, Phys. Rev. Lett. **79**, 3608 (1997).
[10] Y. Yamamoto, K. Kubo, and H. Toki, Prog. Theor. Phys. **98**, 95 (1997).
[11] G. Bunce, N. Saito, J. Soffer, and W. Vogelsang, Annu. Rev. Nucl. Part. Sci. **50**, 525 (2000).
[12] K. Krueger *et al.*, Phys. Lett. B **459**, 412 (1999).
[13] F.Z. Khiari *et al.*, Phys. Rev. D **39**, 45 (1989).
[14] H. Huang, Ph.D. thesis, Indiana University, 1995.
[15] H. Huang *et al.*, Phys. Rev. Lett. **73**, 2982 (1994).
[16] M. Bai, Ph.D. thesis, Indiana University, 1999.
[17] M. Bai *et al.*, Phys. Rev. Lett. **80**, 4673 (1998).
[18] M. Bai *et al.*, Phys. Rev. Lett. **84**, 1184 (2000).
[19] L. Blumberg *et al.*, Brookhaven National Laboratory report BNL 24508R, 1979.
[20] K.A. Brown *et al.*, Brookhaven National Laboratory report BNL-63857, 1997.
[21] D.G. Crabb *et al.*, Nucl. Phys. **B121**, 231 (1977).
[22] H. Spinka *et al.*, Nucl. Instrum. Methods Phys. Res. **211**, 239 (1983).
[23] C.E. Allgower *et al.*, Nucl. Instrum. Methods Phys. Res. A **399**, 171 (1997).
[24] C. Ohmori *et al.*, Nucl. Instrum. Methods Phys. Res. A **278**, 705 (1989).
[25] J. Bystricky *et al.*, Lett. Nuovo Cimento Soc. Ital. Fis. **40**, 466 (1984).
[26] N. Akchurin *et al.*, Phys. Lett. B **229**, 299 (1989).
[27] M. Borghini *et al.*, Phys. Lett. **36B**, 501 (1971).
[28] A. Gaidot *et al.*, Phys. Lett. **61B**, 103 (1976).
[29] D.P. Grosnick *et al.*, Nucl. Instrum. Methods Phys. Res. A **290**, 269 (1990).
[30] D.P. Grosnick *et al.*, Phys. Rev. D **55**, 1159 (1997).
[31] E. Byckling and K. Kajantie, *Particle Kinematics* (Wiley, London, 1973), see p. 222.
[32] A.I. Pavlinov, IHEP 98-37, Protvino, 1998.
[33] R. Brun *et al.*, ''GEANT Users Guide,'' Program Library W5013, CERN, 1993.
[34] D. Antreasyan *et al.*, Phys. Rev. D **19**, 764 (1979).
[35] B.Z. Kopeliovich, hep-ph/9801414; and (private communication).
[36] B.E. Bonner *et al.*, Phys. Rev. D **41**, 13 (1990).
[37] S. Saroff *et al.*, Phys. Rev. Lett. **64**, 995 (1990).
[38] V.D. Apokin *et al.*, Phys. Lett. B **243**, 461 (1990).
[39] T. Eichten *et al.*, Nucl. Phys. **B44**, 333 (1972).
[40] A.V. Efremov and O.V. Teryaev, Sov. J. Nucl. Phys. **36**, 140 (1982); J. Qiu and G. Sterman, Nucl. Phys. **B378**, 52 (1992); S.J. Brodsky, P. Hoyer, A.H. Mueller, and W.-K. Tang, *ibid.* **B369**, 519 (1992).
[41] J. Qiu and G. Sterman, Phys. Rev. D **59**, 014004 (1999).
[42] A.V. Efremov and O.V. Teryaev, Phys. Lett. **150B**, 383 (1985).
[43] P.G. Ratcliffe, Eur. Phys. J. C **8**, 403 (1999).
[44] D. Sivers, Phys. Rev. D **41**, 83 (1990); **43**, 261 (1991); M. Anselmino, M.E. Boglione, and F. Murgia, in *Proceedings of the 11th International Symposium on High Energy Spin Physics, Bloomington, 1994*, edited by K.J. Heller and S.L. Smith, AIP Conf. Proc. No. 343 (AIP, New York, 1994), p. 446.
[45] M. Anselmino, M. Boglione, and F. Murgia, Phys. Lett. B **362**, 164 (1995); M. Anselmino and F. Murgia, *ibid.* **442**, 470 (1998).
[46] J. Collins, Nucl. Phys. **B396**, 161 (1993); J.C. Collins, S.F. Heppelmann, and G.A. Ladinsky, *ibid.* **B420**, 565 (1994).
[47] M. Anselmino, M. Boglione, and F. Murgia, Phys. Rev. D **60**, 054027 (1999).
[48] M. Boglione and E. Leader, Phys. Rev. D **61**, 114001 (2000).
[49] X. Artru, J. Czyzewski, and H. Yabuki, Z. Phys. C **73**, 527 (1997).
[50] C. Boros, L. Zuo-tang, and M. Ta-chung, Phys. Rev. Lett. **70**, 1751 (1993).
[51] S.M. Troshin and N.E. Tyurin, Phys. Rev. D **52**, 3862 (1995); **54**, 838 (1996).
[52] L. Zuo-tang and M. Ta-chung, Z. Phys. A **344**, 171 (1992).
[53] L. Zuo-tang and C. Boros, Int. J. Mod. Phys. A **15**, 927 (2000).
[54] N.I. Kochelev, JETP Lett. **72**, 481 (2000).
[55] T.A. DeGrand and H.I. Miettinen, Phys. Rev. D **23**, 1227 (1981); **24**, 2419 (1981); **31**, 661(E) (1985).
[56] B. Andersson, G. Gustafson, and G. Ingelman, Phys. Lett. **85B**, 417 (1979).
[57] J. Soffer and N.A. Torngvist, Phys. Rev. Lett. **68**, 907 (1992).
[58] R. Lednicky, Sov. J. Nucl. Phys. **43**, 817 (1986); P. Cea *et al.*, Phys. Lett. B **193**, 361 (1987); M.G. Ryskin, Sov. J. Nucl. Phys. **48**, 708 (1988); T. Fujita and N. Suzuki, Nucl. Phys. **A503**, 899 (1989); W.G.D. Dharmaratna and G.R. Goldstein, Phys. Rev. D **41**, 1731 (1990); M. Svec, *ibid.* **42**, 2237 (1990).
[59] G.J. Musulmanbekov and M.V. Tokarev, in *Proceedings of the 12th International Symposium on High-Energy Spin Physics, Amsterdam, 1996*, edited by C.W. de Jager *et al.* (World Scientific, Singapore, 1997), p. 464.